Dust Lifting Observations with the Mars Science Laboratory Navigation Cameras

Scott D. Guzewich[1]*, Emily L. Mason[2,1,3], Mark T. Lemmon[4], Claire E. Newman[5], and Kevin W. Lewis[6]

[1]NASA Goddard Space Flight Center; Greenbelt, MD, USA.
[2]University of Maryland Baltimore County, Catonsville, MD, USA.
[3]Center for Research and Exploration in Space Science and Technology II, NASA/GSFC, Greenbelt, MD, USA
[4]Space Science Institute, Boulder, CO, USA.
[5]Aeolis Research, Pasadena, CA, USA.
[6]Johns Hopkins University, Baltimore, MD, USA.

*Corresponding author: Scott D. Guzewich (scott.d.guzewich@nasa.gov)

Key Points:

- The Mars Science Laboratory Navigation Cameras have taken 1,260 dedicated image sequences searching for dust lifting
- Approximately 42.7% of all sequences and 9.5% of all images show active dust lifting
- Dust lifting in Gale Crater most frequently occurs on sand-covered surfaces

Abstract

Martian dust lifting is believed to occur through two primary mechanisms: dust devils and wind stress forced dust lifting. Gale Crater's varied terrain and meteorology provide a unique *in situ* perspective on martian dust lifting, with the Mars Science Laboratory Curiosity rover passing through both conditions and locations detrimental to dust lifting (e.g., the crater floor) and those with active sand motion and frequent dust lifting (e.g., the Bagnold Dunes). Between L_s = 248° in Mars Year 33 and L_s = 51° in Mars Year 37, over ~3.5 Mars years and 2,300 sols, the rover's Navigation Cameras took 1,260 dedicated image sequences to search for dust lifting. Approximately 42.7% of all sequences, and 9.5% of the total images, have shown active dust lifting, both dust devils and linear/straight-line wind stress dust lifting. 79% of dust lifting events are classified as dust devils, while ~16% are linear wind stress dust lifting and the remainder are of an indeterminate type. We analyze this large catalog of dust lifting events to provide ground truth on theoretical and model expectations of dust lifting and show that dust lifting in Gale Crater occurs throughout the martian year, is strongly peaked in frequency near solar noon (even after accounting for observational biases), and that dust lifting shows an affinity for sand-covered surfaces which highlights the importance of saltating sand grains for martian dust lifting in both dust devils and wind stress forced lifting.

Plain Language Summary

Airborne dust is an important control on the modern martian climate. Dust is lifted into the air by two primary mechanisms: dust devils (rotating columns of air that are also common in dry areas on Earth) and the force of straight-line winds acting on dust-covered surfaces. The Mars Science Laboratory Curiosity rover Navigation Cameras have taken regular movies to search for dust lifting in Gale Crater. Approximately 42.7% of all sequences, and 9.5% of the total images, have shown active dust lifting and we analyze this large catalog of events to better understand the mechanisms and conditions that lift dust into the air on Mars. We find that dust lifting in Gale Crater is more strongly clustered near solar noon than previously expected from analyses of air pressure and that dust lifting often occurs on sand-covered terrains, suggesting that motion of sand grains across the surface supports dust lifting.

1 Introduction

Over nearly 11 Earth years and more than 5 Mars years, the Mars Science Laboratory (MSL) Curiosity rover has traversed >10 km horizontal distance (with a track length of >30 km) and ~700 m vertically from Bradbury Landing (within the floor or trench of Gale Crater) up the slopes of Gale Crater's central mound, Mt. Sharp/Aeolis Mons. Throughout the mission, Curiosity has taken observations in support of one of its core science objectives: studying the modern environment (Vasavada, 2022). These have employed a variety of instruments and observation sequences to study dust lifting and depositional processes within Gale Crater.

The Rover Environmental Monitoring Station (REMS) measures pressure, air and ground temperature, wind speed and direction (although these sensors were damaged on landing and ceased operation altogether ~2.4 Mars years into the mission), ultraviolet (UV) radiation in several wavelength bands, and relative humidity (Gómez-Elvira et al., 2012). Soon after landing, REMS pressure measurements showed transient drops consistent with convective vortices passing over or near the rover (Harri et al., 2014; Moores et al., 2015a; Steakley and Murphy, 2016; Kahanpää et al., 2016, Newman et al., 2019). In a convective boundary layer forced by strong solar surface heating (e.g., Mason et al., 2023), wind shear and vertical motion produce vertically-oriented and stretched vorticity columns with central low pressure and a radially-oriented wind field (Ryan and Carroll, 1970; Rennó et al., 1998; Metzger et al., 1999; Greeley et al., 2003; Ringrose, 2005; Balme and Greeley, 2006; Neakrease and Greeley, 2010). These convective vortices form along the edges, and especially at the corners, of daytime convective cells, where strong updrafts exist. If mobile surface dust is present, and if near-surface atmospheric conditions (such as the wind stress due to tangential winds around the vortex) are sufficient to initiate dust lifting, this convective vortex can become visible as a "dust devil." REMS can also indirectly and opportunistically measure the dustiness of these convective vortices by concurrent decreases or increases in UV radiation (through shadowing or reflecting sunlight, respectively), but such searches early in the mission found comparatively few convective vortices with a distinct UV radiation signal (Steakley and Murphy, 2016; Kahanpää et al., 2016; Ordóñez-Exteberria et al., 2018; Kahanpää and Viúdez-Moreiras, 2021). On longer timescales, REMS has also measured seasonal variations in dust deposition and removal on the UV photodiodes located on the rover's deck (Vicente-Retortillo et al., 2018; Vicente-Retortillo et al., 2020).

Dust devils are believed to play an important role in the modern martian climate. Based on modeling and orbital data analysis, dust devils may supply ~50% of the dust to the global atmosphere and maintain a moderate background level of atmospheric opacity throughout the martian year (Basu et al., 2004; Cantor et al., 2006; Balme and Greeley, 2006; Guzewich et al., 2015). Understanding the spatial and temporal (e.g., diurnal and seasonal) variation of dust devil occurrence and characteristics, and the link between atmospheric conditions and the amount of dust raised by these vortices, therefore informs our understanding of the entire martian climate and dust cycle. The remainder of dust in Mars' atmosphere is believed to be lifted through linear surface wind stress processes (Bagnold 1936, 1941; Kahre et al., 2017; Whelley and Greeley, 2008; Kok et al., 2012; Guzewich et al., 2015), which also likely raise the most dust within the larger-scale dust storms that can occasionally reach planetary scales. However, while vortex and dust devil activity is expected to decrease during a storm once widespread increased opacity reduces the convective forcing at the surface, recent modeling (Wu et al., 2021) and observations by the Perseverance rover (Lemmon et al., 2022) suggest that vortex and dust devil activity actually increases early on within the active lifting center of a storm, when opacity is still horizontally heterogeneous and can boost convective strength. Thus dust devils may also have a small role (relative to straight-line wind stress dust lifting) to play in the initial onset of dust storms.

Another area of uncertainty is the precise mechanism by which dust is lofted by martian vortices. In addition to the tangential wind around the vortex, which produces surface wind stress peaking at the vortex edge, other factors may also contribute to dust lifting, ranging from a so-called 'suction' effect due to the central pressure drop, to increased electrostatic forces on the dust particles within the fast-moving vortex. These factors may explain why the wind stresses associated with vortex / dust devil lifting appear to be smaller than those predicted for linear wind stress lifting (e.g., Baker et al., 2021). The role of sand in raising dust within vortices also remains a major question. Sand particles are larger than dust particles, and while this makes them heavier it also makes them far less cohesive, hence they are expected to be set into motion more easily (i.e., to have a lower wind stress threshold). It has long been suggested that saltating sand particles, which fall back to the surface and add the force of this impact to the background wind stress, may be necessary to raise dust in linear winds (e.g., Sagan and Bagnold, 1975). However, the importance of this 'sand-blasting' effect in raising dust within dust devils has not been explored to date.

The coarse global spatial variation of dust devils has been studied with the benefit of both an orbital perspective (e.g., Thomas and Gierasch, 1985; Fischer et al., 2005; Stanzel et al., 2006; Cantor et al., 2006; Whelley and Greeley, 2008; Reiss et al., 2014; Fenton et al., 2016) and a variety of landers. While the Viking Landers detected the signature of convective vortices in pressure data (e.g., Ryan and Lucich, 1983; Ringrose et al., 2003), no dust devils were seen in imagery. The Pathfinder lander was the first to detect convective vortices in both the pressure signal and concurrent images of dust devils (Schofield et al., 1997; Metzger et al., 1999). The Spirit and Opportunity rovers, while lacking a pressure sensor, both saw dust devils in dedicated image sequences, with far more observed at Spirit's field location in Gusev Crater (Greeley et al., 2006; Greeley et al., 2010). Despite the InSight lander measuring abundant strong (up to 9.2 Pa) convective pressure vortices (Lorenz et al., 2020), and even seeing occasional newly created surface tracks, InSight never definitively imaged a dust devil or dust lifting event (Spiga et al., 2021; Lorenz et al., 2021a; Baker et al., 2021; Charalambous et al., 2021; Jackson et al., 2021). Like InSight, Phoenix detected the signature of vortices in pressure data, but without visible detections (Ellehøj et al., 2010). The disparity between Gusev Crater (Spirit) and Elysium Planitia (InSight) is also apparent in the frequent and reliable "cleaning" events that prolonged the energy production from Spirit's solar panels, while InSight eventually succumbed to low power failure due to the lack of such cleaning events (Lorenz et al., 2021b). The Mars 2020 Perseverance rover, however, immediately imaged frequent dust devils and wind gust-driven dust lifting events in Jezero Crater (Newman et al., 2022; Lemmon et al., 2022) and concurrently measured their signals in temperature, wind, air pressure and radiation signatures (Hueso et al., 2023; Jackson, 2022; Toledo et al., 2023), surface albedo (Vicente-Retortillo et al., 2023), and even sound (Murdoch et al., 2022).

Studies of the wide variation in dust lifting frequency across landing sites have not yet utilized the unique perspective of Curiosity's horizontal and vertical traverse across a wide variety of geological surfaces ranging from hard sandstone bedrock to basaltic sand dunes. Like its predecessors, Curiosity regularly searched for dust devils and dust lifting events in image sequences after landing, and despite detections of convective vortices in REMS pressure data, only a single dust devil was seen over the first 360 sols of the mission (Moores et al., 2015a). As Curiosity continued its drive toward Mt. Sharp, a further 18 dust lifting events were imaged through Sol 1561 (Lemmon et al., 2017), which still suggested that dust lifting was quite infrequent within Gale crater. However, since ~Sol 1500, Curiosity has taken systematic dust devil imaging campaigns with the Navigation Cameras (Navcam) and Mast Cameras (Mastcam) and has seen far more abundant dust devils and dust lifting events. For these reasons, we start our analysis at this point. The increase in imaged dust lifting event frequency has been concurrent with increased REMS pressure detections of convective vortices (Kahanpää et al., 2018; Newman et al., 2019; Ordóñez-Etxeberria et al., 2020; Uttam et al., 2022) and appears to be associated with local-scale environmental factors that are more favorable for convective vortex/dust devil formation along the slopes of Mt. Sharp (largely increased sensible heat flux; Newman et al., 2019).

In this paper, we present and analyze a rich catalog of dust devils and dust lifting events seen by the Curiosity rover in Gale Crater over more than 3.5 Mars years (corresponding to MSL mission Sols 1500-3800). These events have been seen by dedicated Navcam imaging sequences to identify dust devils and dust lifting events. In Section 2 we describe these Navcam image sequences, how dust lifting events are identified and cataloged within them, and what information can be determined from the Navcam images alone. Section 3 presents our results, describing the patterns and characteristics of dust devils and dust lifting in Gale Crater. Lastly, Section 4 puts these results in context of Gale Crater meteorology and the broader martian climate and dust cycle, and provides our conclusions.

2 Methods

Curiosity's Navigation Cameras are build-to-print copies of those on Spirit and Opportunity (Maki et al., 2003; Maki et al., 2012). The Navigation Camera system consists of four Navigation Cameras mounted on top of the rover's mast, two of which are operating at any given time based on which side of the rover's redundant main computer is operating. The cameras have 45° fields of view (FOV) with a 0.82 mrad/pixel scale (Maki et al., 2012). They have broadband visible (600-850 nm) spectral ranges that return grayscale images. Our analysis uses the radiometrically calibrated "RAS" version of the images available on the NASA Planetary Data System (Maki, 2018). While the Navcam field of view is nominally 1024x1024 pixels, nearly all observations used here are subframed to some degree, particularly in the vertical direction.

Navcam's primary purpose is, self-evidently, to help navigate the rover and identify geologic targets of interest. However, it also has been a capable workhorse science instrument for environmental science. In addition to the observations we discuss focusing on dust devils and dust lifting events, Navcam has routinely executed observations to study clouds (Kloos et al., 2016; Cooper at al., 2018; Campbell et al., 2020) and to measure the line-of-sight opacity within the crater (Moore et al., 2016; 2019; Smith et al., 2019).

In total, we have analyzed 1,260 image sequences taken during Sols 1500-3800, comprising more than 34,500 total images, as listed by Guzewich et al. (2023). A "sequence" is a single packet of Navcam observations composed of multiple images or "frames." These image sequences fall into 3 broad categories: dust devil surveys, dust devil movies, and "Shunt Prevention ENV Drop-In" (SPENDI) sequences. Dust devil surveys are 24-image sequences that take 3 images in each of 8 azimuthal pointing directions, covering the entire 360° FOV around the rover. There are ~13 second pauses between each image in a triplet and slews between azimuths take ~32 seconds. Prior to Sol 1815, 6- and 8-image dust devil surveys were also used. Dust devil movies have fixed azimuthal and elevation pointing (relative to the local planetary coordinate system) and come in 2 types: short and long. Short dust devil movies are 21-image sequences with ~13 second pauses between images. Before Sol 1587, 4-frame short dust devil movies were used (with longer ~70 second pauses between frames). Long dust devil movies are 45-image sequences with ~13 second pauses between images within a triplet grouping and ~93 second pauses between each triplet. SPENDI activities, first used on Sol 2937, are image sequences judged to be safe over many sols without needing to be edited. They can therefore be added late in the planning process to use excess energy that would otherwise be thermally shunted (Hayes et al., 2023). A variety of SPENDI sequences exist with 48-192 images that are combinations of dust devil survey images and "suprahorizon" cloud movie images (e.g., Kloos et al., 2016; Hayes et al., 2023). Of the 1,260 total image sequences, 620 are surveys, 581 are movies, and 59 are SPENDIs.

Downlinked Navcam images are typically compressed in some fashion to manage the rover's data volume, whether lossy or lossless (Maki et al., 2012). Over the course of the mission, the compression on individual dust devil imaging sequences has varied from highly compressed (e.g., 2 bits/pixel) to losslessly compressed, based on the mission's overall data management posture at the time of imaging. In very broad terms, sequences earlier in the mission were more compressed whereas lossless compression has been used more often later in the mission, following the arrival of the Mars Atmosphere and Volatile Evolution (MAVEN) and Trace Gas Orbiter (TGO) missions that have provided additional data relay capability. In practice, higher compression makes identifying dust lifting more challenging, particularly for distant dust lifting events. As compression increases, far-field dust lifting is reduced to the noise level in the mean-frame subtracted images (see next paragraph) whereas kilometers-distant dust lifting can be confidently identified in losslessly compressed images.

Few dust lifting events are visible to the naked eye in the raw or radiometrically calibrated images. This indicates that most dust lifting events have low opacities with limited contrast to the sky or nearby terrain. We employ the mean frame subtraction (MFS) technique (e.g., Moores et al., 2015a; Kloos et al., 2016; Campbell et al., 2020; Hayes et al., 2023; see also Metzger et al., 2000) to isolate changing features within a single image sequence. The mean-frame is created for each individual image grouping (e.g., a dust devil survey image triplet at a given azimuth or all 21 frames of a short dust devil movie). We additionally flag pixels with values more than 4 standard deviations away from the mean MFS pixel value. This serves to remove cosmic ray hits to the detector and "hot pixels." Flagged areas are typically very small and visual inspection confirms this flag does not remove any dust lifting events. Figures 1 and 2 show a dust devil survey and short dust devil movie, respectively, with their unprocessed and MFS images (see also Supplemental Movies 1 and 2).

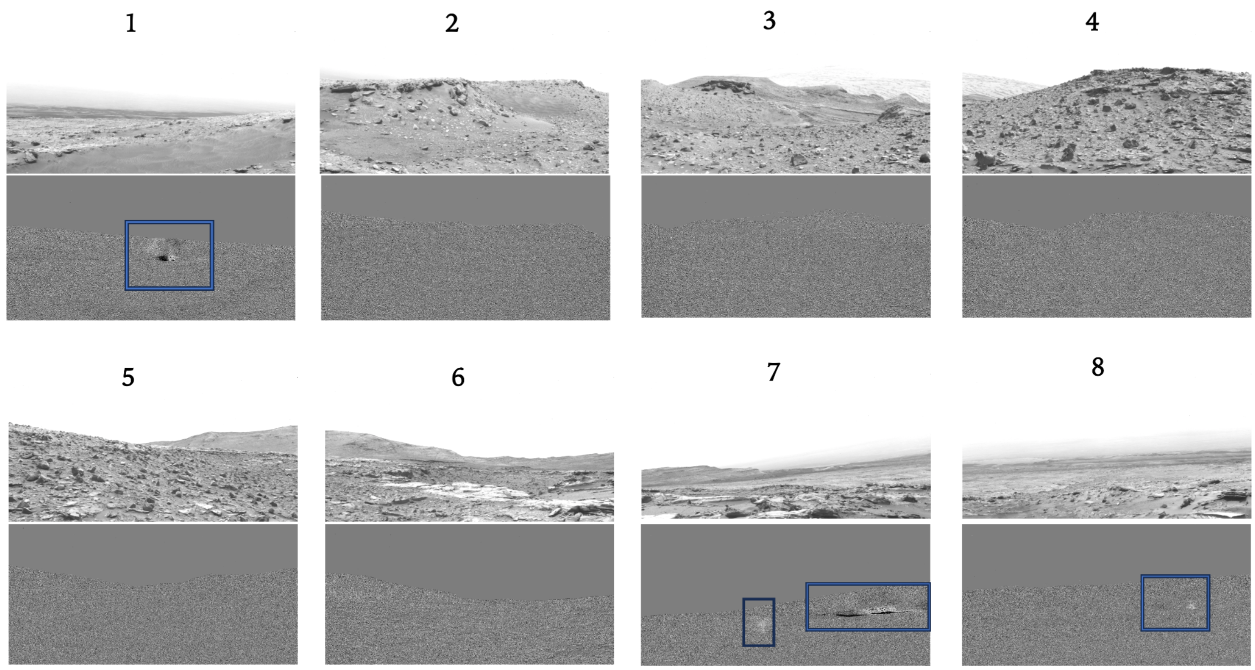

Figure 1. One unprocessed image from each of the eight unique azimuth pointings of the Sol 3451 Navcam dust devil survey with an associated mean-frame subtracted image below each unprocessed image. Dust lifting can be seen in the mean-frame subtracted images 1 and 7-8 highlighted with boxes.

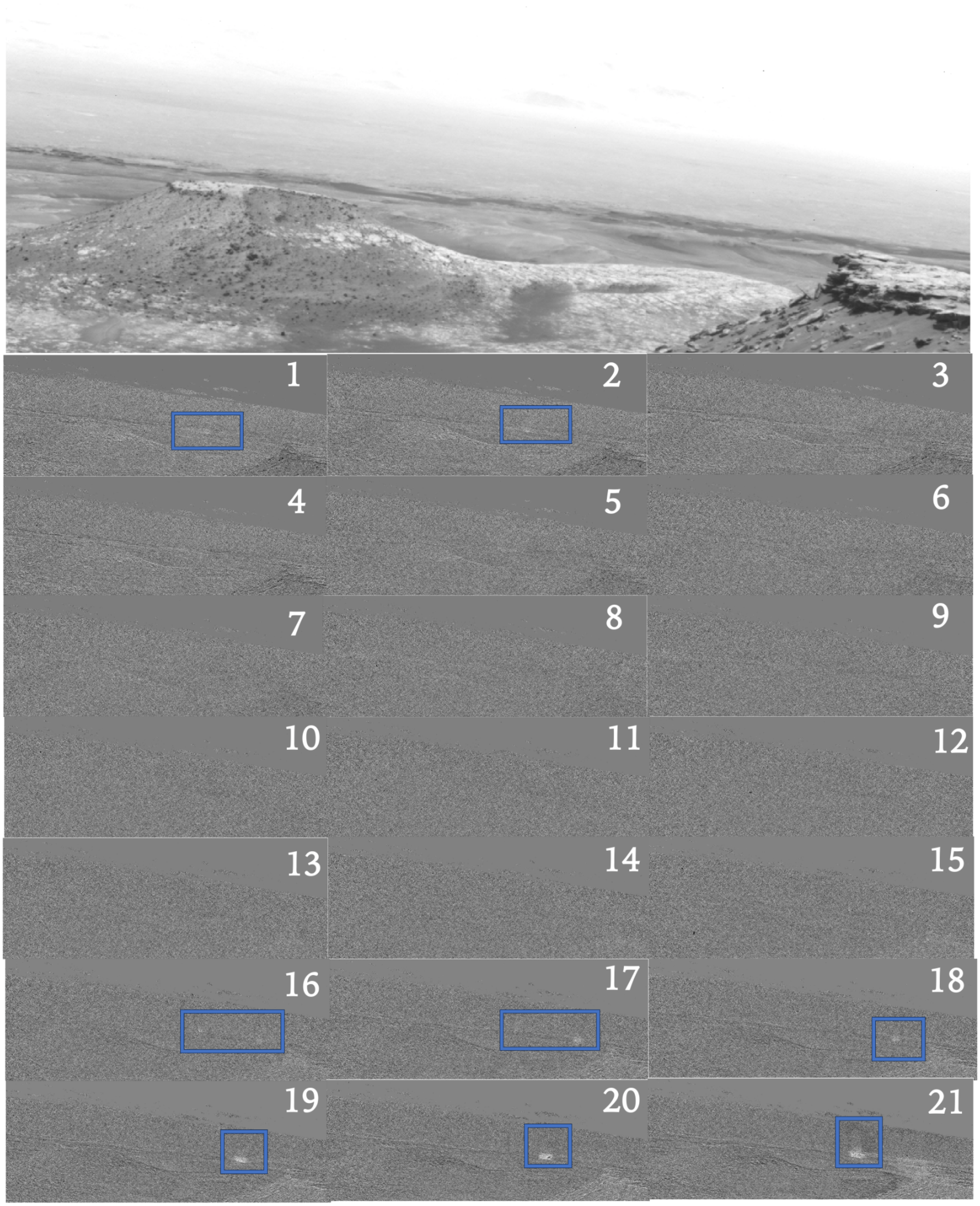

Figure 2. One unprocessed image from the Sol 2717 short dust devil movie (top) and the associated 21 mean-frame subtracted images (bottom). Dust lifting can be seen in mean-frame subtracted images 1-2 and 16-21 highlighted with boxes.

After generating MFS images for each sequence, the images are visually inspected for dust lifting events. Dust lifting events can be seen in MFS images 1, 7 and 8 in Figure 1 and MFS images 1-2 and 16-21 in Figure 2. In general, lofted dust is brighter than the surrounding surface and darker than the sky and thus appears whiter in the MFS against the ground and darker or invisible against the sky. While most movies showed that brightness pattern clearly, surveys sometimes had more complex patterns due to using only 3 images in the MFS. For instance, Figure 1 shows two dust lifting events that are seen in both positive (bright, dusty areas) and negative (dark areas within the mean frame that was subtracted). Particularly in MFS images of an image triplet (compared to MFS over an entire 21-frame image), the dust devil or dust lifting event's motion produces alternating black and white patterns from MFS image to MFS image (Figure 1 panel 7, Figure 12). Additionally, care must be taken to note changing illumination and shadow patterns due to terrain features over the course of a particular image sequence. For example, note the dark color of the nearby cliff in the lower right corner of MFS images 1-5 in Figure 2, which then becomes visibly brighter in MFS images 16-21.

MFS images with visually confirmed dust lifting events are then processed manually through a graphical user interface (GUI) written in the IDL programming language: the dust lifting event's pixel locations are identified, the event is classified (as either a dust devil, wind-stress lifting event, or an indeterminate dust lifting event), and a subjective confidence level is assigned. Dust devils are visually identified by their columnar shape and vertical extent (e.g., Supplemental Movie 1), while straight-line wind stress events typically have very little apparent vertical extent and larger horizontal spread (e.g., Supplemental Movie 2). Strictly speaking, dust may be lifted in dust devils by the wind stress of strongly rotating air on the surface that initiates saltation and splashing of dust particles into the air. So while wind stress may be the agent causing dust lifting for both dust devils and straight-line or linear wind gusts, for the rest of this manuscript, we term straight-line or linear wind-drive dust lifting as "wind stress" dust lifting to differentiate it from rotating dust devils.

3 Results

3.1. Dust Lifting Occurrence Statistics

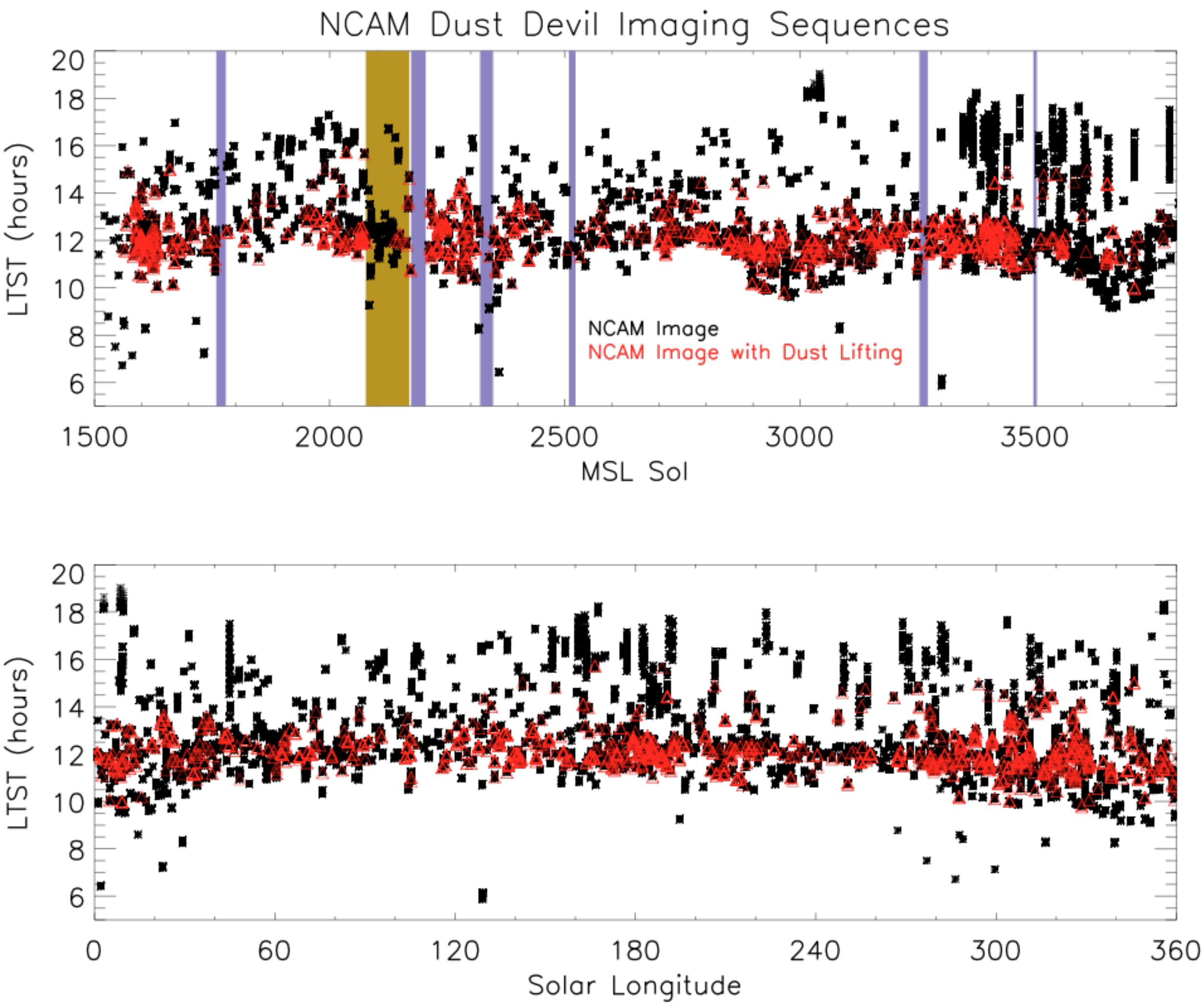

Figure 3. Complete record of Navcam dust devil imaging sequences by local true solar time (LTST) and MSL mission sol (top) or by solar longitude (bottom). Black asterisks indicate each Navcam image and red triangles indicate images with observed dust lifting. The vertical lavender bars represent significant gaps in observations due to rover safe modes and other events, while the gold bar indicates the MY34 global dust storm.

Over the ~3.5 Mars years analyzed, Curiosity has taken a dedicated Navcam sequence to monitor dust lifting about once every 1.8 sols on average. The rate has not been constant over time based on mission priorities and other factors (e.g., Figure 4), but represents a substantial investment of mission resources to create this record. Figure 3 presents the entire record of Navcam dust devil imaging sequences taken over this period and the identified dust lifting observations within those. In total, 3,225 images were identified that included dust lifting (a dust devil, wind-stress dust lifting, or an indeterminate type) representing ~9.5% of all images taken within the 1,260 sequences and >34,500 images. Out of the 1,260 sequences, 538 (~42.7%) included dust lifting. Dust devils comprised ~79% of all dust lifting events, while ~16% were classified as linear wind stress lifting. For all subsequent analysis, it is important to be mindful of the inherent observational biases within these data. Navcam dust devil observations are far from systematically distributed in time-of-day, season, and pointing direction. While some attempt has been made to mitigate these in the design of observations (e.g., dust devil surveys image in all 360° of azimuth), these biases are still strongly present in the data. Indeed, the relative lack of dust lifting detections prior to Sol 1500 (e.g., Moores et al., 2015a) is at least partially due to the Navcam dust devil image sequences pointing almost exclusively north over the crater floor rather than uphill toward the Bagnold Dune fields and areas with more conducive conditions for dust lifting (e.g., Newman et al., 2019). Curiosity's traverse through the complex terrain of Gale Crater (as opposed to the comparatively flat ground at the Spirit, Opportunity, InSight, and even Perseverance landing sites) has also resulted in a highly changeable viewshed where locations with frequent dust lifting have moved in-and-out of view from one sol to another.

A variety of patterns are present in the data, some of which represent real meteorological information and some of which are driven by rover planning considerations. The clustering of both images and dust lifting detections near local noon (12:00 LTST) is a combination of both. REMS pressure vortices occur most frequently at noon or in early afternoon when solar energy input is highest (e.g., Newman et al., 2019) and this pattern is also present in visible dust lifting detections. But there is also a strong bias toward scheduling Navcam dust devil image sequences near noon, both because of that scientific expectation that noon and early afternoon is the most active dust lifting time of day and due to the pattern of the rover's daily activity sequences. Curiosity typically has a midday (meaning hours around local noon) "science block", when a variety of science activities occur, and this is when the majority of Navcam images are scheduled. Biases in the viewsheds used for the images are also present, with the science and operations team preferentially pointing movies in directions where previous dust lifting has occurred and dust lifting is more easily visible (even in MFS images) against darker or sandier surfaces. There is also a somewhat sinusoidal variation on the earliest time of Navcam sequences in Figure 3, seen three times in the top panel (for each full Mars year) and then folded together on the bottom panel. This is driven by orbital and seasonal factors that determine when the rover's daily activities begin. Because of this, the sampling of mid-to-late morning dust devil imaging sequences is far less systematic than that in the early-to-mid afternoon and our statistics are accordingly biased. Since Sol 2937, the inclusion of SPENDIs (which are included into plans at a late stage, once resources and the periods of power shunting are known, and without science team input) has greatly increased coverage of the late afternoon and early evening (pre-sunset) periods. This is because their goal - to productively use up excess power - is satisfied by the rover staying awake and imaging at this later time of day. Conversely, dust devil observations planned by the science team tend to occur earlier, especially in sols where power is limited. This is both due to the usual midday timing of the primary science blocks, and the difficulty of adding science block time later in the day in most sols.

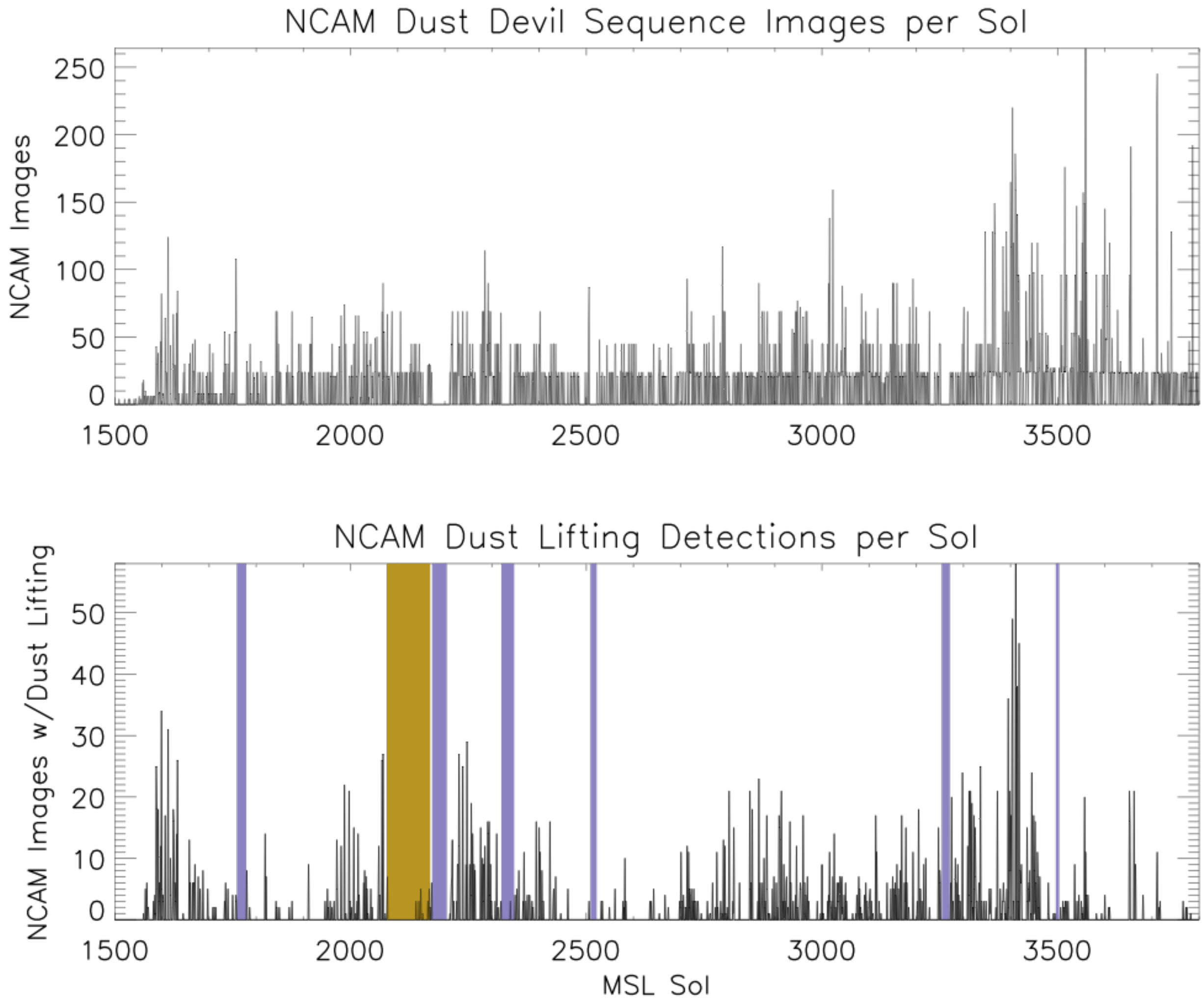

Figure 4. Number of Navcam dust devil sequence images per sol (top) and number of images with observed dust lifting (bottom) by MSL mission sol with the vertical bars as described in Figure 3.

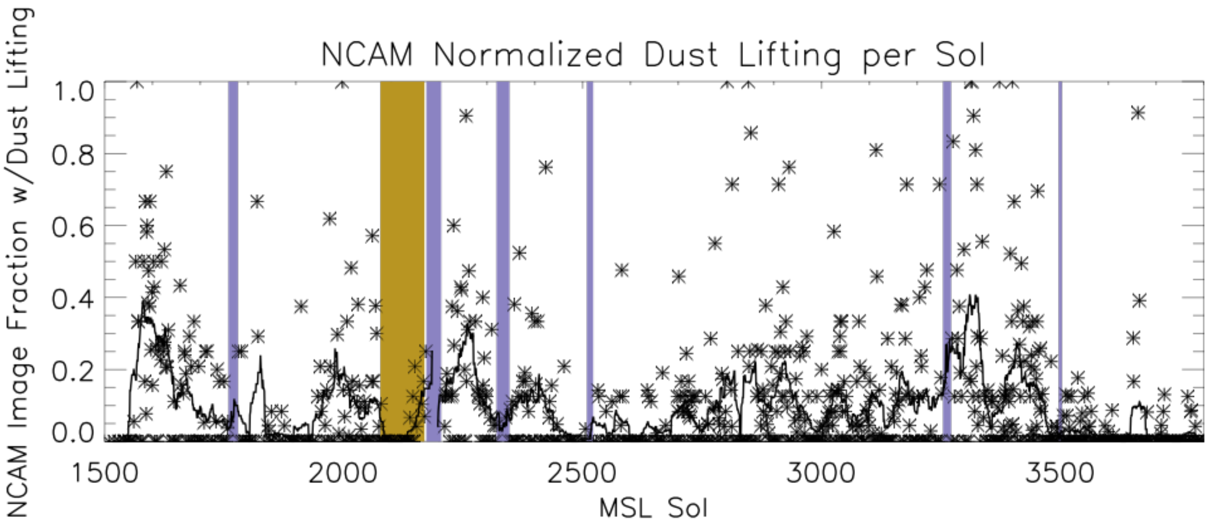

Figure 5. The fraction of Navcam dust devil sequence images with observed dust lifting by MSL mission sol. The black line is a smoothed 30-sol running mean value with the vertical bars as described in Figure 3.

Figure 4 presents the same data in a different manner, to highlight the number of images taken per sol in a Navcam dust devil movie, survey, or SPENDI activity and the corresponding number of images with dust lifting within each sol. It's clear the most frequent number of images per sol is 21 or 24, corresponding to the most common types of Navcam dust devil movies and surveys, respectively. The addition of SPENDI sequences causes a noticeable increase in images after Sol 3000. Still, as mentioned above, most sols do not have any Navcam dust devil image sequences.

The number of dust lifting detections per sol is highly variable, with zero being the most common by far, but with values ranging up to a maximum of 58 images with dust lifting on Sol 3411. Note that in the bottom panel of Figure 4, no effort is made to distinguish between a single dust devil that persists for an entire 21-frame movie or 21 unique dust devils over the same movie. It also does not double-count images with multiple distinct concurrent dust lifting events.

Dividing the two panels of Figure 4 results in Figure 5's normalized dust lifting activity values. This provides a more consistent view of dust lifting activity across the entire mission, despite the highly variable frequency at which Navcam image sequences are taken. The median value of the running 30-sol smoothed curve in Figure 5 is 9% with a mean value of 10% across the entire period of analysis. Two time periods, however, have 30-sol frequency values near 0.4 (40%): near Sols 1600 and 3400. Sol 1600 was soon after more frequent and dedicated Navcam dust devil movies and surveys began to be scheduled. Curiosity was crossing the active Bagnold Dune field during this time near "Ogunquit Beach." Hence, the rover directly observed that such an active dune field is conducive to dust lifting and aeolian motion and despite fewer images per sol, those images frequently included dust lifting. This dust lifting included both dust devils and straight line wind-stress forced dust lifting. Straight line winds causing sand saltation and wind-stress dust lifting in a location with active aeolian motion is expected, but dust devils were more common during this time period within the Bagnold Dune field. Near Sol 3400, Curiosity was on top of the Greenheugh Pediment with a long downslope viewshed over the Sands of Forvie sandsheet, Glen Torridon valley, and the Bagnold Dune field. Essentially, all of the most productive dust lifting locations (see below) of the entire mission were in view concurrently. There have also been two distinct time periods with limited dust lifting activity: Sols 2450-2600 and the current period starting near Sol 3600. The current period (Sol 3600-present) is easily explainable by Curiosity's location in the Marker Band valley, with a limited viewshed and terrain that appears less conducive to dust lifting with a lack of broad sand coverage and more frequent bedrock and boulder-covered terrain. However, the Sol 2450-2600 period is not easily explained by issues of viewshed or location. During that time, the rover was in the Glen Torridon valley, which in other seasons had frequent dust lifting. Indeed, more frequent dust lifting occurred both before and after this period, with the rover only a relatively short distance away. This period of limited dust lifting is best explained by seasonal declines in meteorological conditions and solar forcing that are conducive to boundary layer convection. Sols 2450-2600 covers $L_s = 45\text{-}110°$, when solar forcing is minimized at Gale Crater. This matches well with predictions by Newman et al. (2019) showing dust devil activity is lowest during this season due to reduced thermal forcing and shallower planetary boundary layer depth during the afternoon.

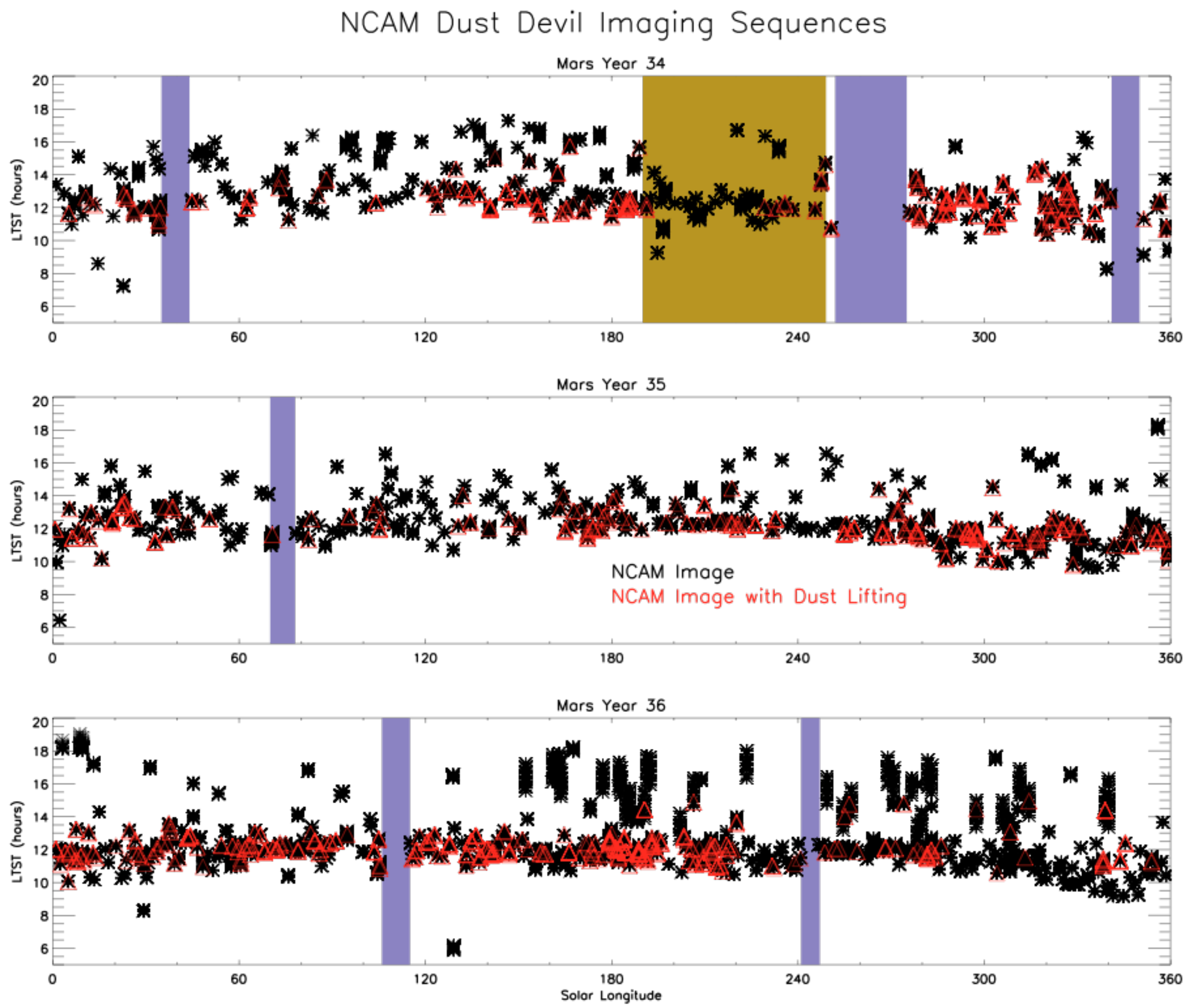

Figure 6. Navcam dust devil imaging sequences by local true solar time and solar longitude for Mars Years 34 (top), 35 (middle), and 36 (bottom). Black asterisks indicate each Navcam image and red triangles indicate images with observed dust lifting with the vertical bars as described in Figure 3.

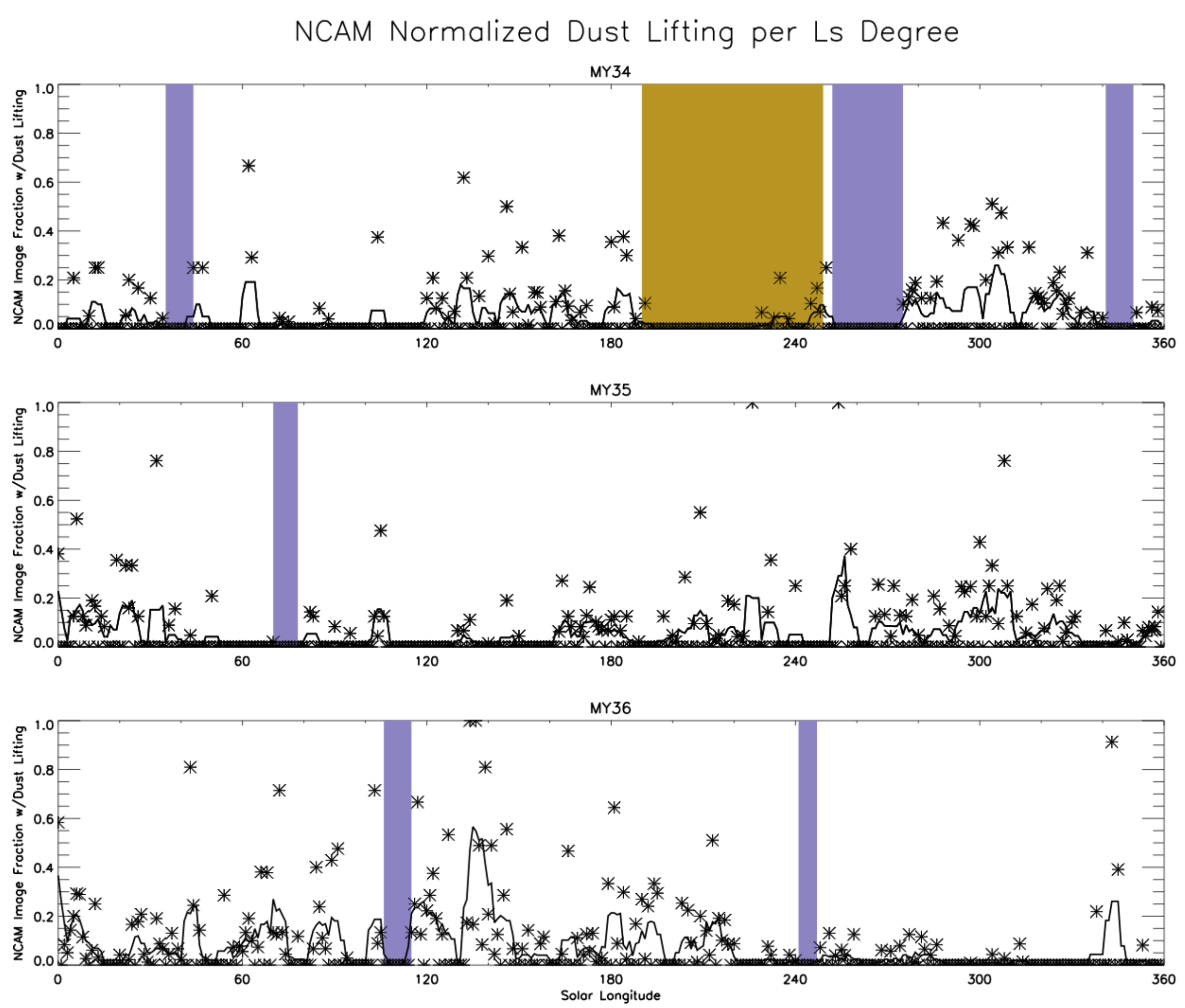

Figure 7. Normalized dust lifting frequency (percent of Navcam dust devil sequence images with dust lifting events, asterisks) by 1° of solar longitude over Mars Year 34 (top), Mars Year 35 (middle), and Mars Year 36 (bottom). Solid black lines are 5° of solar longitude running smoothed means with the vertical bars as described in Figure 3.

Figure 3 shows that there are clusters of more frequent dust lifting near L_s = 180° and between L_s = 270-330°, with somewhat fewer dust lifting detections near southern hemisphere winter solstice (L_s = 90°), but with no time of year devoid of dust lifting. Figures 6 and 7 show the three complete Mars years of our analysis period: Mars Years (MY) 34-36 in the calendar of Clancy et al. (2003). Our analysis period starts at L_s = 248° in MY33 (mission Sol 1500) and runs to L_s = 51° (mission Sol 3800) in early MY37. Moores et al. (2015a) discussed the initial single dust lifting detection in MY31 at the beginning of the mission on the Gale Crater floor and Lemmon et al. (2017) found another handful in late MY32 and early MY33 (slightly overlapping with this work). Hence, Figures 3-7 cover well over 99% of all observed dust lifting within Gale

Crater. Additional dust lifting that is occasionally visible in Navcam image sequences dedicated to studying water ice clouds, or in Mast Camera dust devil movies, are excluded from our analysis.

Substantial interannual variability is present in Figures 6 and 7. However, much of this is driven by the rover's location through this period and its viewshed biases toward areas that are more or less favorable for dust lifting (as described both above and below). MY34 includes the global dust storm, which almost entirely suppressed dust lifting activity within Gale Crater for a period of months (Guzewich et al., 2019). MY36's seasonal variation is strongly driven by rover location. The strong cluster of dust lifting activity between L_s = 120°-180° that year was during a period when the rover had an excellent viewshed, as described above, and there was a high frequency of Navcam dust devil imaging sequences (although as seen in Figure 7, this time period had some of the highest normalized dust lifting frequency of the entire mission). The near dearth of dust lifting detections after L_s = 210° that year occurred when the rover traversed into "Marker Band Valley," where the viewshed was limited and very few nearby dust lifting events occurred. Of those three years, MY35 likely best samples the "true" meteorological variations in dust lifting within Gale Crater. Throughout that year, Curiosity had a good viewshed through the "Glen Torridon" region (Sullivan et al., 2022), there was only a single period with no data collection (solar conjunction), and there were no major dust storms.

These seasonal variations are seen more clearly in Figures 7 and 8. Again MY35 likely represents the closest depiction to the true seasonal variation of dust lifting within Gale Crater with a relatively smooth variation between a broad peak in dust lifting in southern hemisphere spring and summer (L_s = 180-360°) and a minimum near L_s = 60-150°. Comparable seasonal variation is also seen in model predictions and REMS pressure vortex detections (Newman et al., 2019). The total observation period has some suggestion of this pattern, with the fewest detections occurring between L_s =30-120° throughout the mission, but significant observation biases are inherently included. MY34 has a 60° of solar longitude gap between L_s = 210-270° due to both the MY34 global dust storm and a long safe mode event immediately following the storm. That reduction in what otherwise would have likely been an active time period results in the total period detections being noticeably double-peaked over the year. MY36 has the inherent viewshed biases discussed above (particularly after L_s = 220°), producing a very anomalous seasonal pattern that is likely not meteorologically-driven. By comparison, dust lifting observations from the Spirit rover were more clustered in season with pronounced gaps with very little activity, but a peak in dust lifting activity in southern hemisphere spring and summer (note Spirit's landing site in Gusev Crater was at 14.56°S, compared to 4.59°S for Curiosity) was clear for multiple Mars years (Greeley et al., 2006; 2010), which generally aligns with Curiosity's complete record and MY35 in particular.

Although linear wind stress dust lifting events were a small fraction of total observed dust lifting events, we note that they have a distinctly different seasonal distribution (see Figures S1 and S2). Wind stress dust lifting events are strongly concentrated near L_s = 180° through the mission, however the inherent viewshed biases present in these data may be concentrated in this smaller portion of dust lifting events. Both in MY34 and MY36, the time period near L_s = 180° included broad views of the Bagnold Dunes and the majority of all linear wind stress dust lifting events were observed in just these two narrow time windows. In MY34, the start of the global dust storm and subsequent rover safe mode precluded dust lifting and observations following $L_s \sim 190°$, while in MY36, the rover's route into Marker Band Valley limited dust lifting detections as discussed above and below. Still, MY35, without any of those obvious meteorological, technological, or geological impediments also saw a peak of linear wind stress lifting near $L_s = 180°$. Future modeling efforts should investigate whether meteorological conditions in this season are more conducive to strong straight-line winds.

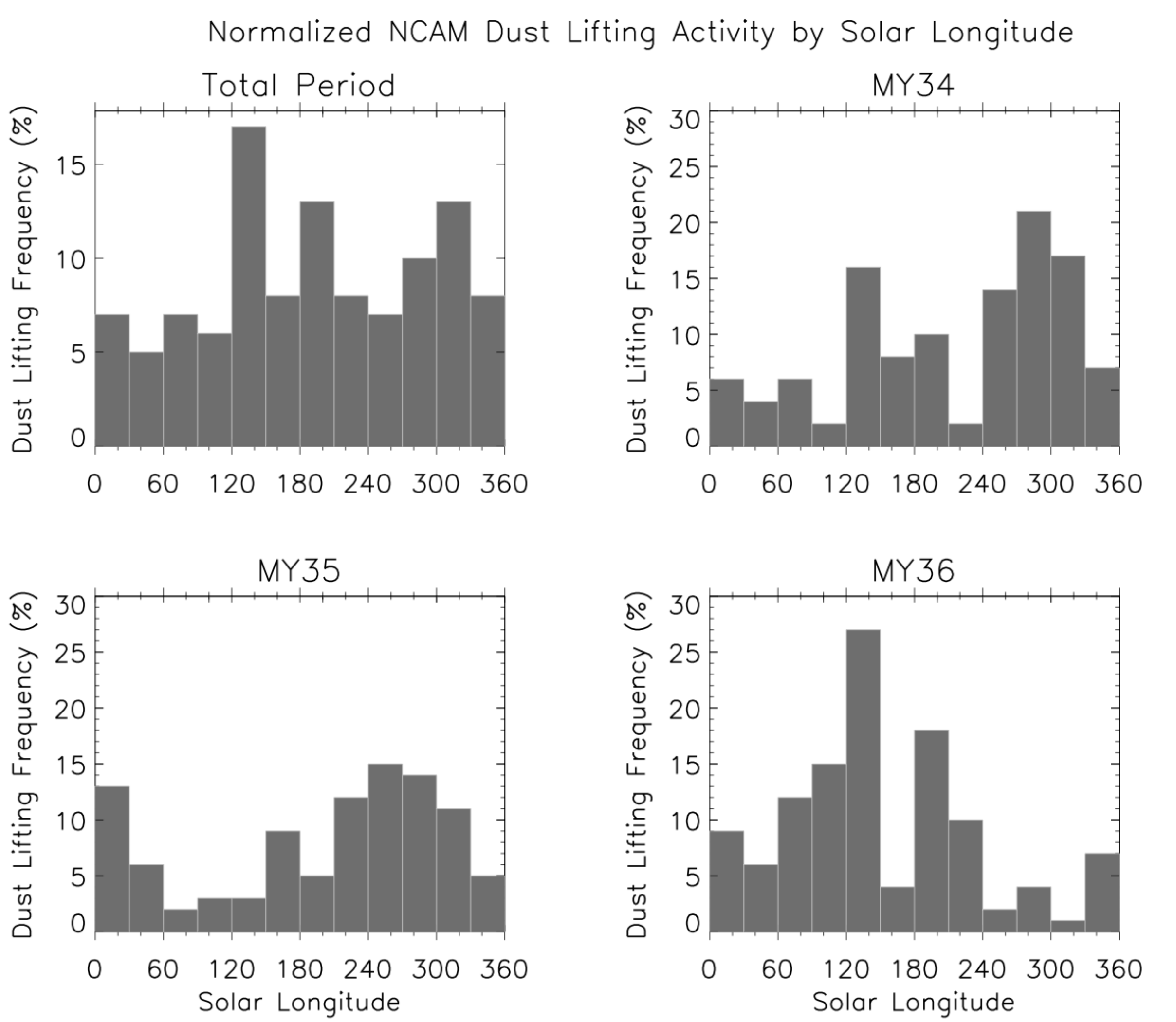

Figure 8. Normalized histograms of dust lifting frequency (percent of Navcam dust devil sequence images with dust lifting events) by solar longitude over the entire period of analysis (top left), Mars Year 34 (top right), Mars Year 35 (bottom left), and Mars Year 36 (bottom right).

Far less interannual variability is present in the distribution of dust lifting activity by time of day. The observed dust lifting activity histogram across the entire period presented here (Figure 9) is strongly Gaussian with a peak very close to solar noon. Each full year also has a Gaussian peak, although MY36 alone substantially influences the occurrence distribution for the entire mission. MY34 and MY35 are more broadly peaked between 1130-1300 LTST. As mentioned above, the relative lack of observations in the mid-late morning results in fewer detections between 0930-1130 than what might truly be occurring in Gale Crater and what occurs in early-mid afternoon.

The earliest dust lifting detection was just before 1000 LTST (although there are very few image sequences before 1000 LTST) and the latest near 1530 LTST. This is a narrower time range than was seen in Gusev Crater by Spirit, particularly for the afternoon times (Greeley et al., 2010). Spirit also was biased through the same rover planning cadence considerations as Curiosity with relatively fewer observations and detections in mid-late morning. Still, the relative lack of activity in the afternoon in Gale Crater is notable. REMS pressure vortices show a broader peak of activity with significant activity continuing into the afternoon (Newman et al., 2019). As seen in Figures 3 and 6 also, this lack of detections in the early to mid afternoon is robust. Throughout the entire mission, there have been regular Navcam observations in the afternoon between 1300-1600 LTST, and even occasionally later into the evening. SPENDI observations, in particular, are almost exclusively scheduled during the 1400-1800 time period. To demonstrate this lack of dust lifting activity in the afternoon, we focus on the period around Sol 3300-3500 (late southern winter through early spring in MY36). During this period, Curiosity had an excellent north-pointing viewshed of the Sands of Forvie sandsheet, Glen Torridon valley, and the Bagnold Dunes and saw abundant dust lifting activity during the middle of the day (note the peaks at this time in Figure 9 for MY36). There were also frequent SPENDI observations in the afternoon and evening, which also, in part, included north-pointing azimuths. Despite that, only a handful of dust lifting events were seen during this period in the mid-late afternoon. This stands in contrast to model predictions of dust devil activity and REMS pressure vortex detections (Chapman et al., 2017; Newman et al., 2019), which imply a peak in the early afternoon and continued activity through ~1600 LTST before a sharp decline after 1600. Linear wind stress dust lifting events have a very similar distribution in local time to the entire dust lifting event catalog.

Normalizing by observation frequency (Figure 10) also does not remove this relative lack of afternoon dust lifting activity (see also Figure S3). Figure 10 shows a more gradual decline in dust lifting frequency during the afternoon compared to the raw counts shown in Figure 9, but dust lifting frequency still falls to 10% or below after 1300 LTST. The source of this disparity must be meteorological (dust availability doesn't change diurnally), but it is beyond the scope of this work to determine the cause. We speculate that upslope and downslope flows, that even in mesoscale models are not fully resolved, may more effectively dissipate developing vertically-oriented vorticity at these times, or cause them to be narrower and thus raise dust over a smaller area (making them less visible), but additional modeling is required to help resolve this question. Still,

Figure 10 does help resolve some of the bias in observation times and hence shows a broader peak of dust lifting activity of generally 10-20% of images between 1100-1300 LTST.

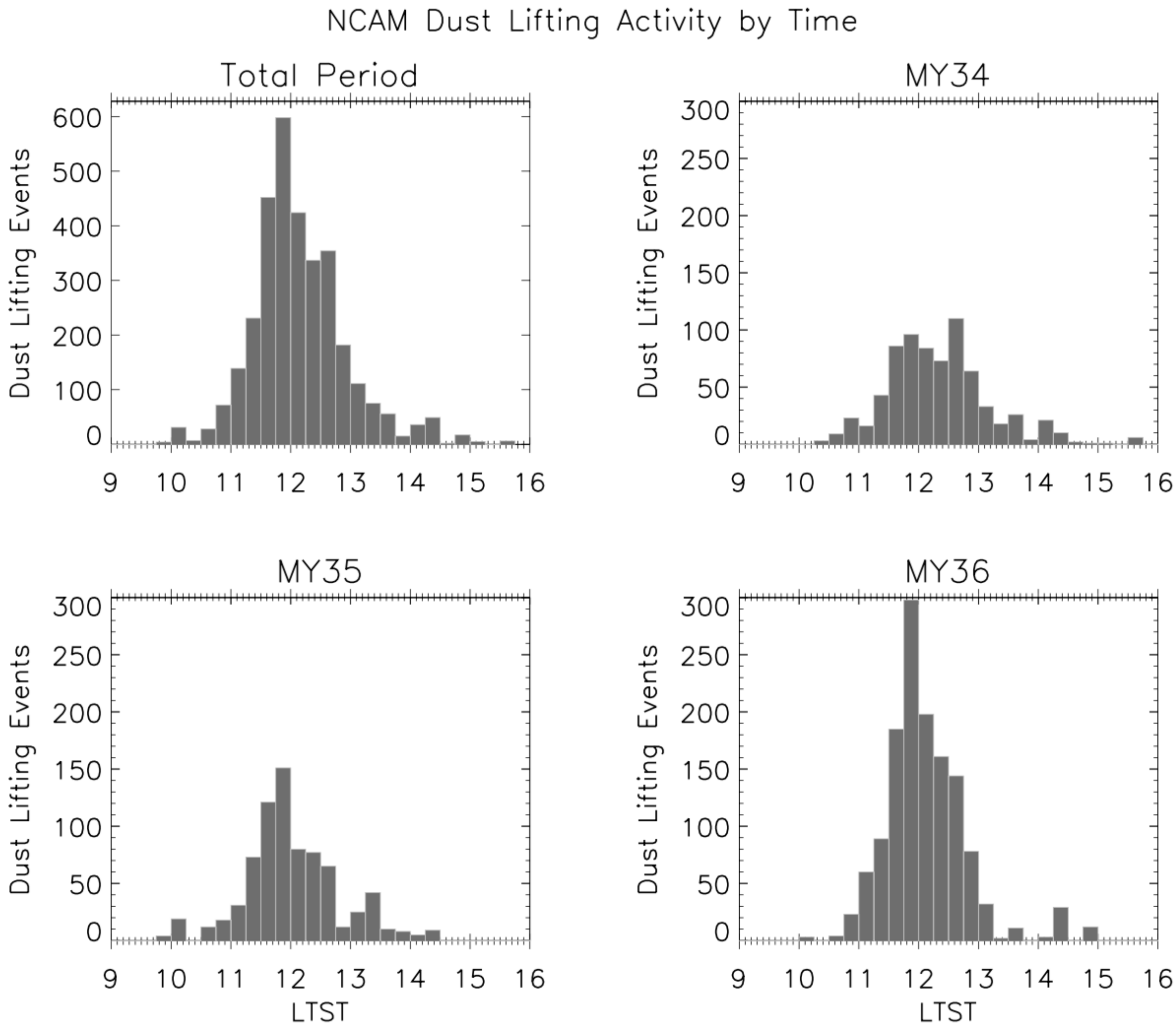

Figure 9. Histograms of dust lifting events by local true solar time over the entire period of analysis (top left), Mars Year 34 (top right), Mars Year 35 (bottom left), and Mars Year 36 (bottom right).

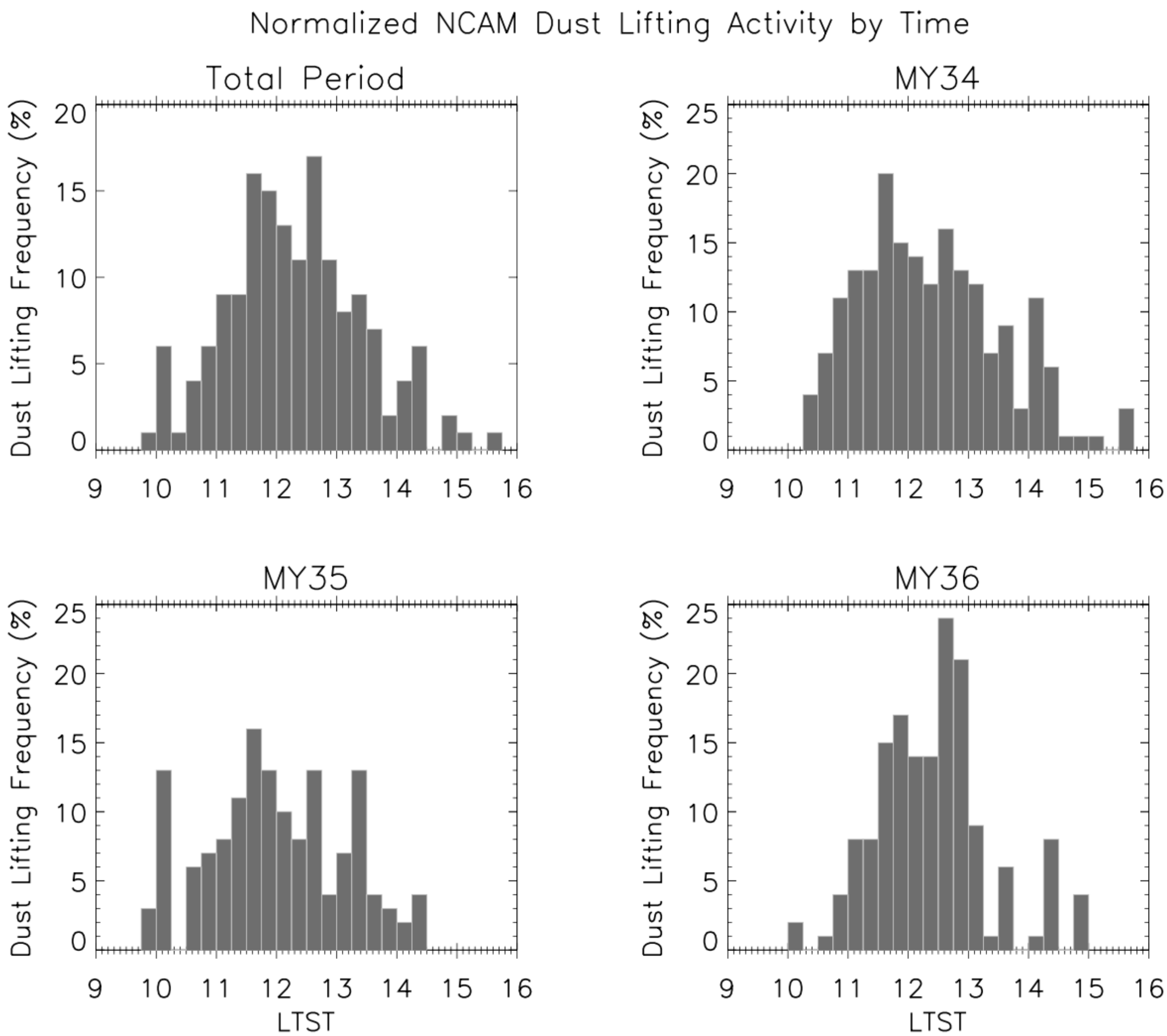

Figure 10. Histograms of normalized dust lifting events (percent of Navcam dust devil sequence images with dust lifting events) by local true solar time over the entire period of analysis (top left), Mars Year 34 (top right), Mars Year 35 (bottom left), and Mars Year 36 (bottom right).

3.2. Dust Lifting Locations and Surface Properties

Beyond the background meteorological conditions, surface properties and dust availability are integral to understanding dust lifting physics on Mars. Therefore, localizing dust lifting events within Gale Crater is a necessary step to understand what surfaces can lift dust and are dust sources for the atmosphere. This is far more challenging than with similar efforts for Pathfinder (Ferri et al., 2003) and Spirit (Greeley et al., 2006; 2010). First, Curiosity has moved through much more complex terrain at an often faster pace than its predecessors. Second, there have been few or no dust devil tracks identified from orbit along or near Curiosity's traverse route (Ordóñex-Exteberria et al., 2018). We attempt to localize observed dust lifting events using two different methods.

A systematic way to localize observed dust lifting is to simply report the azimuthal direction in which each dust lifting event occurs, and we do this in Figure 11. We can determine the azimuth of each pixel in a given image using the camera's pointing azimuth, CAHVOR (Camera center, Axis, Horizontal, Vertical, Optical, and Radial distortion vectors) model (Di and Li, 2004; Maki et al., 2012), and spherical geometry. Figure 11 shows that the predominant directions of observed dust lifting have been incredibly variable over the 2,300 sols we analyze. Note that these data have not been normalized to pointing direction frequency in any way. We divide the 2,300 sol period into seven periods based on the rover's locations. We note again that inherent viewshed biases are present here, particularly for dust devil "movies," where the science and operations team preferentially pointed toward directions of known previous dust lifting activity.

The Sol 1500-1610 period, when the rover was within or just north of the Bagnold Dunes, shows dust lifting preferentially toward the south and east directions. Specifically, most dust lifting was occurring near and along the Bagnold Dunes with very few detections elsewhere. As Curiosity passed through the Bagnold Dunes and approached the Vera Rubin Ridge (Sols 1610-1900), there was the greatest diversity in dust lifting directions for the entire mission. While there was a notable tendency for detections through the Bagnold Dune field (SW and NE directions in Figure 11), there were also a number of detections toward the Vera Rubin Ridge (S and SE directions). As the rover moved to the top of Vera Rubin Ridge during Sols 1900-2300, a period which also spanned the MY34/2018 global dust storm and subsequent long rover safe mode event, the predominant directions of observed dust lifting reverted to a more bimodal distribution again. Again, dust lifting was most abundant over the Bagnold Dunes (N directions) with the second most common over the Glen Torridon valley and upslope toward higher terrain (S directions).

Around Sol 2300, the rover descended the Vera Rubin Ridge into the Glen Torridon valley. Geologically and mineralogically, Glen Torridon is the clay-rich region along the slopes of Mt. Sharp that helped define the mission's original scientific objectives (Bennett et al., 2023). Glen Torridon is bounded on its north side by the Vera Rubin Ridge, which also obscured the rover's view of the Bagnold Dune field. Glen Torridon is bounded on the southern side by the increasingly higher terrain up the slopes of Mt. Sharp. Over the next 1000+ sols, numerous Navcam sequences showed that it is a region with abundant dust lifting, with both dust devils and wind-stress dust lifting. Throughout this long time period, the rover saw frequent dust lifting toward the northeast, along the orientation of the Glen Torridon valley (southwest to northeast). As the rover moved east through Glen Torridon (Sols 2800-3120), the directions of dust lifting became modestly more dispersed. As the rover moved east, it passed north of the Sands of Forvie sand sheet, where dust lifting events were also observed, and it also had a broader viewshed of the western terminus of the valley along the Greenheugh Pediment. Once the rover turned back to driving generally southwestward (Sols 3120-3330), dust lifting was only observed toward the northeast, through Glen Torridon and over the Sands of Forvie sand sheet.

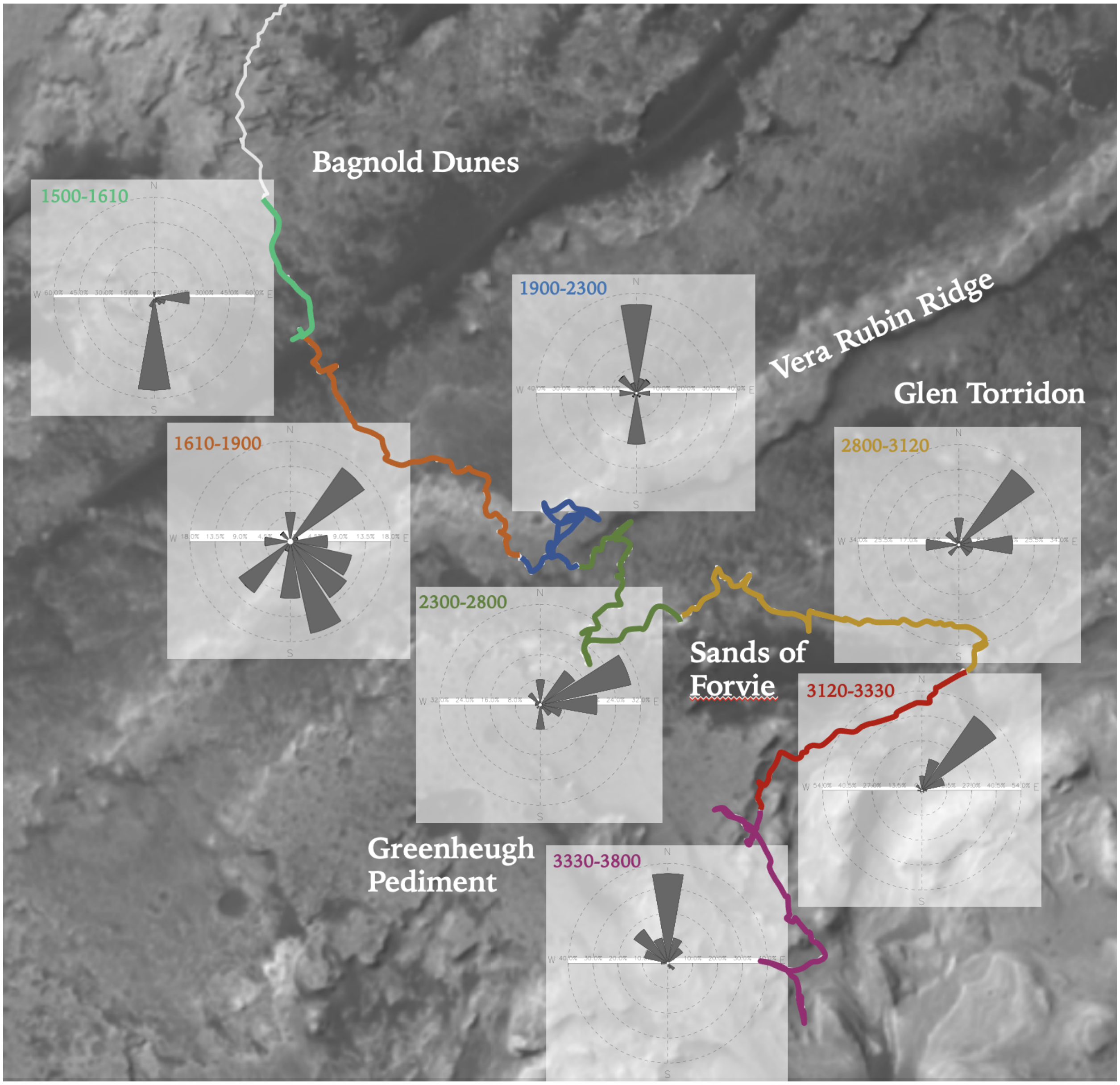

Figure 11. Wind rose diagrams of azimuth of observed dust lifting events over seven color-coded time periods (MSL Sols) overlaid on orbital imagery of Gale Crater with the Curiosity rover's traverse route and major terrain features labeled. Rover traverse and background from: https://mars.nasa.gov/maps/location/?mission=Curiosity.

The final section of Figure 11, Sols 3330-3800, covers the steep ascent up the slopes of Mt. Sharp with highly variable viewsheds. Twice the rover attempted to drive out onto the Greenheugh Pediment and had to retreat due to hazardous driving conditions. However, those sojourns onto the Pediment provided incredibly productive viewsheds for dust lifting observations. During those periods, the rover again had a view of the Bagnold Dunes (toward the north) while also having much of Glen Torridon within sight (toward the north and northeast). This combination produced very frequent dust lifting detections in north-pointing directions. However, the final ~250 sols of this period saw the fewest dust lifting detections of any comparable-length period. During this time, as mentioned above, the rover was in Marker Band Valley, with a very constrained viewshed and apparently unfavorable local conditions for dust lifting. What little dust lifting has been seen in this period has been almost exclusively toward the southeast (upslope) direction.

After Sol 3400, Navcam dust devil movies were modified in an attempt to get precise locations for dust lifting events as part of standard image processing. The MSL Engineering Camera team routinely calculates distances to objects (out to a maximum distance of ~400 m from the rover) when stereo images are taken by Navcam (Maki et al., 2012). Thus, a stereo image pair was added to the dust devil movies to allow ranging. However, no dust lifting events were seen within the calculated range of the stereo dust devil movies between Sol 3400-3800. With that stereo image-based method unsuccessful to date, we use a second method to localize dust lifting. Our second method of dust lifting localization is a best-effort attempt to get approximate locations (i.e., distance as well as direction) for some events to help understand the spatial variability of dust lifting within Gale Crater. This localization, which is non-trivial and is subject to increasing error with increasing distance between an individual dust lifting event and the rover, allows us to understand the surface properties that are more conducive to dust lifting in Gale Crater.

Using the pointing azimuth and elevation of the Navcam sequence, spherical geometry, and the associated CAHVOR model (Di and Li, 2004; Maki et al., 2012), we calculate a vector between Navcam and each pixel within a dust lifting event identified by hand in the IDL GUI. This vector is then projected out onto Gale Crater's topography as defined by the High-Resolution Imaging Science Experiment (HiRISE) digital terrain model (DTM) (Kirk et al., 2008). The closest point to the rover represents the base of the dust lifting event. Each localization solution is then visually validated based on identifying terrain features for plausibility. This method is subject to a variety of potential errors due to rover localization, misidentification of pixels within the IDL GUI, and the complex terrain of Gale Crater. For example, frequently the true base of a dust devil is obscured behind terrain and thus this method will produce spurious results and the result is discarded. Driven by these different factors, quantifying the uncertainty in an individual location is not possible, but we can say that the errors are almost entirely in the radial direction rather than azimuthal. Those radial errors can plausibly be tens of meters to even kilometers, depending on the specific dust lifting events, as the rover was often kilometers distant when they were observed. Only a small subset of all identified dust lifting events are successfully localized using this method and discussed below, but we believe it is a sufficiently robust sample to draw meaningful conclusions. In total, we have 1,875 localizations, however note that in many cases the same individual dust lifting event is localized across multiple images as it moves.

We demonstrate the output of this localization method in Figure 12. A dust devil is seen plainly in the mean-frame subtracted image with two dark representations of the dust devil in the subsequent two images (i.e., the dust devil is moving left to right across the images). For this dust devil survey, the rover was pointing towards the northeast downslope with a view of the Sands of Forvie (dark sandsheet in the center of the unprocessed image) and the Glen Torridon valley. After identifying the dust devil in our IDL GUI, the vector to it is projected out onto the HiRISE DTM resulting in the location shown on the left panel of Figure 12.

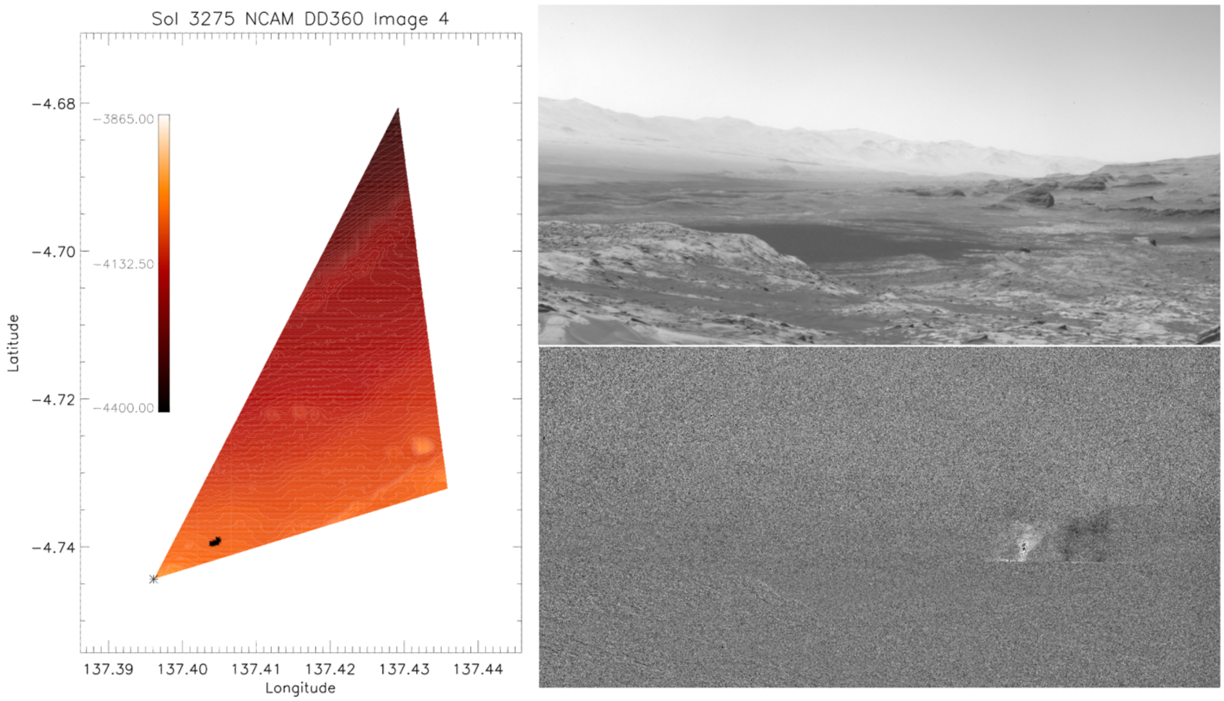

Figure 12. Example of dust lifting localization routine with the fourth image of the Sol 3275 dust devil survey. The localized pixels are plotted on the HiRISE DTM topography with the rover's position at the time of the sequence indicated by the asterisk (left). The unprocessed image is on the top right with the mean-frame subtracted image below it showing a bright dust devil and two dark representations of the dust devil in the subsequent fifth and sixth images of the sequence.

Figure 13 shows locations for dust lifting events identified in 1,875 Navcam images overlaid on the HiRISE DTM. While this only represents a small subset of identified dust lifting events, it represents a reasonable sample covering the entire Sol 1500-3800 period of observation and across different pointing azimuths. Starting at the north end of the figure, there are scattered dust lifting locations on the crater floor, both for dust devil and wind stress dust lifting. These crater floor events were all seen at great distance from the rover and thus have some of the largest uncertainties on precise location. South of the crater floor lies the southwest–northeast oriented Bagnold Dune field which was consistently among the most favorable areas for dust lifting. Figure 13 represents the dominance of dust lifting within and near the Bagnold Dunes well with a high density of locations between approximately -4.69°S and -4.72°S. Both dust devils and wind stress dust lifting are common in the dune field, although there is a notable reduction in plotted locations near the center of the DTM (~137.39°E). This is due to the fact that this portion of the dune field was mainly in view during the period when the rover was on top of the Vera Rubin Ridge, and that time period included both the global dust storm and subsequent extended safe mode event, resulting in fewer dust lifting observations.

The Vera Rubin Ridge cuts across the DTM with a distinct paucity of dust lifting events on top of the ridge itself. However, clustered against the southern edge of the ridge is the greatest cluster of dust lifting locations through the Glen Torridon valley and its vicinity between approximately -4.71°S and -4.75°S and in the eastern 3/5ths of the DTM. As mentioned above when discussing Figure 11, Glen Torridon was in view for the majority of the observation period and was a productive region for dust lifting detections throughout the rover's traverse through it. This included both dust devils and wind stress dust lifting, although wind stress dust lifting is notably more common in the Bagnold Dunes and along the sides of the western edge of the Vera Rubin Ridge. South of Glen Torridon and higher along the slopes of Mt. Sharp, there are only scattered dust lifting locations identified, many of which were seen at great distance from the rover. Some of this relates to the directional observational bias discussed several times previously, but there were also truly less frequent dust lifting occurrences farther upslope on Mt. Sharp. In particular, the eastern half of the Greenheugh Pediment and the Gediz Vallis ridge (the northwest-southeast oriented ridge of higher elevation near -4.77°S and 137.395°E) has been in view of Navcam dust lifting observations numerous times (>1,000 images) with zero dust lifting detections (see also Figure S5). We discuss this more below.

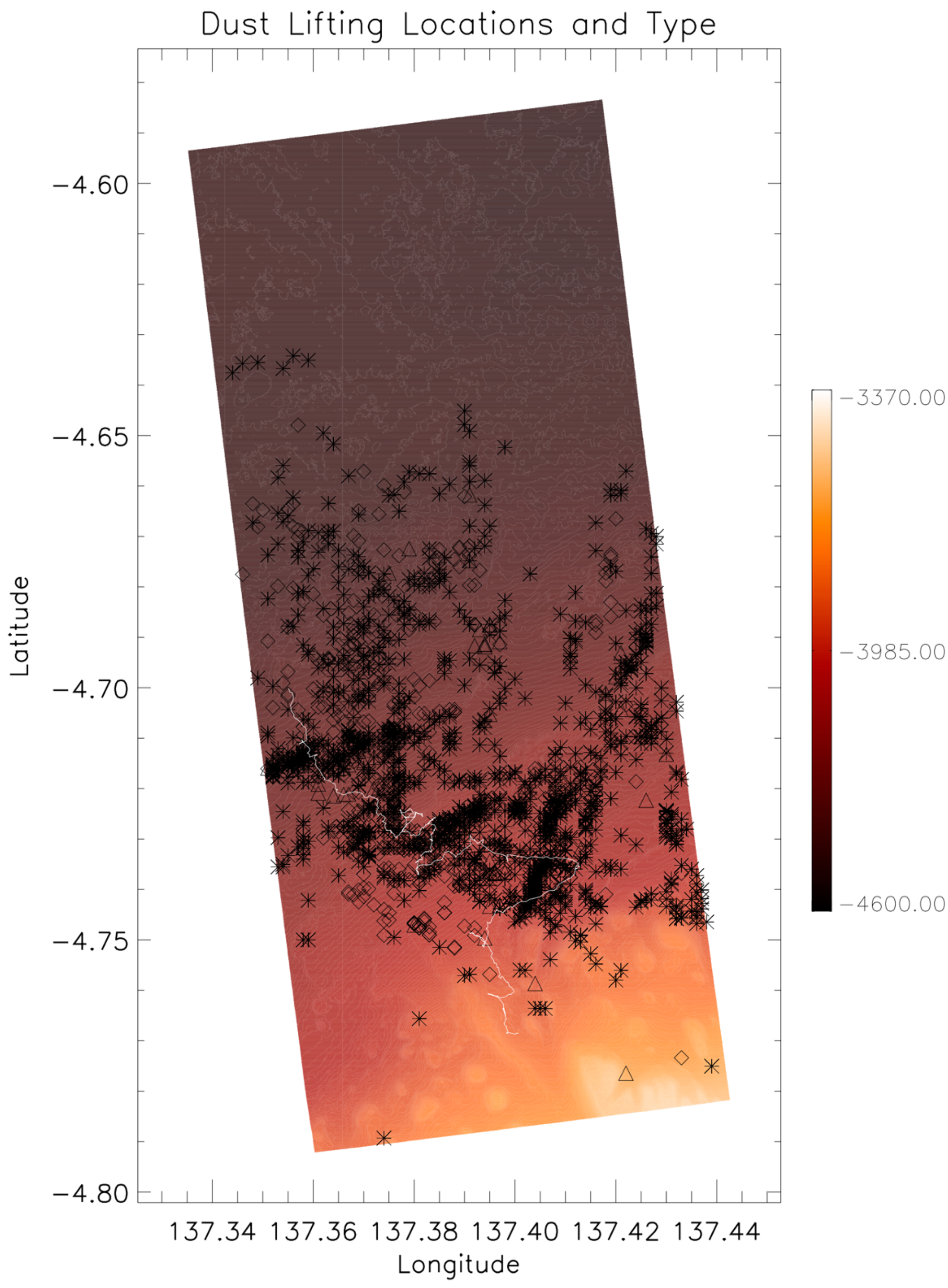

Figure 13. Estimated location of dust lifting events plotted over the HiRISE DTM topography (meters). Asterisks represent dust devils, diamonds represent wind stress dust lifting, and triangles are indeterminate dust lifting events. The thin white line represents the rover's traverse during Sols 1500-3800.

In Figures 14-16 and S4, we plot the dust lifting locations of Figure 13 on a variety of surface maps to identify any patterns or preferences in dust lifting. Figure 14 overlays the locations on a 100 m resolution Context Camera (CTX) mosaic of Gale Crater (Robbins et al., 2023), where dark areas are predominantly sand-covered (e.g., the Bagnold Dunes at the top half of the figure). There are three major sandy regions seen in the CTX image, and the dust lifting locations show a clear preference for them. First, the Bagnold Dunes as previously mentioned. Numerous dust lifting events occurred along and just south of the dunes (where ample surface sand patches are present). Second, in the Glen Torridon Valley just south of the Vera Rubin Ridge there is sand collected against the southern edge of the ridge and occasional sand patches through the valley (Figure S4). Dust lifting is again aligned closely to sandier areas. Lastly, the Sands of Forvie also has a cluster of dust lifting on and near it.

Christian et al. (2022) used the orbital Compact Reconnaissance Imaging Spectrometer for Mars (CRISM) instrument to derive a sand cover index over a small portion of Gale Crater near the rover traverse (see also Viviano-Beck et al., 2014). In Figure 15, we overlay our dust lifting locations on this map. Note that Figure 15 only covers a portion of the Greenheugh Pediment and the edge of the Sands of Forvie. But again, the dust lifting events largely plot on terrain that has more implied sand cover. Even outside the cluster over the Sands of Forvie in the northeast corner of Figure 15, the scattered dust lifting events farther south/upslope show a notable preference for sandier locations.

Figure 16 overlays the dust lifting locations on Thermal Emission Imaging System (THEMIS) qualitative thermal inertia (TI) (Fergason et al., 2006). Brighter areas in Figure 16 indicate higher thermal inertia, while darker areas have lower thermal inertia. Edwards et al. (2018) and Christian et al. (2022) discuss the thermal inertia of terrains near Curiosity's traverse using THEMIS and CRISM observations, respectively. Thermal inertia has also been derived using the rover's onboard sensors (e.g., Vasavada et al., 2017; Martínez et al., 2021). In the vicinity of the traverse, the Bagnold Dunes have some of the lowest thermal inertia (~240 TI units) while the Greenheugh Pediment has the highest (~590) (Edwards et al., 2018). Both features can be seen plainly in Figure 16, as can the Vera Rubin Ridge, which also has comparatively high TI. Newman et al. (2019) noted that TI is a secondary control on dust devil activity and also that TI and albedo can cancel each other out if one is high and the other low (compare Figures 14 and 16). Lower albedo and thermal inertia will cause the surface to warm more rapidly after sunrise, resulting in greater thermal infrared and sensible heating of the lower atmosphere (the latter due to larger surface-to-atmosphere temperature gradients), and hence a greater drive for convection and the formation of vortices and dust devils.

Dust lifting locations plotted in Figure 16 occur on surfaces with a wide range of TI. Indeed, the distribution of thermal inertia of dust lifting locations closely follows the distribution of the entire region, with similar mean and median values. As mentioned previously, very few events were seen on top of the Vera Rubin Ridge itself or on the Greenheugh Pediment (the highest TI regions). One region of particular interest for its lack of dust lifting is the Gediz Vallis Ridge and neighboring eastern portion of the Greenheugh Pediment. The Gediz Vallis Ridge itself has modest TI, lower than the surrounding Greenheugh Pediment (Figure 16), and both areas have relatively little sandcover (Figure 15, see also Bennett et al. (2018)). Despite the modest TI, both areas have zero dust lifting detections in >1,000 images across the observation period.

In combination, we believe Figures 14-16 show that surface sand cover is a key factor in supporting dust lifting by both dust devils and wind stress forcing. Hence, it is the importance of saltating sand grains that can "splash" dust particles into the air (Kok et al., 2012; Neakrease et al., 2016) that is conducive to dust lifting. Plausibly, this sand cover is even more important than a visible layer of surface dust coverage. The dark albedo of sandy areas seen in Figures 11 and 14 indicate that bright martian dust is largely absent relative to other terrains, but what little dust is present on the surface is still available to be lifted when saltating sand particles are present and sufficient to produce visible dust lifting events. Secondly, Figure 16 supports the modeling work of Newman et al. (2019) that thermal inertia is a secondary control on dust lifting and dust devil frequency. The highest TI locations (Vera Rubin Ridge and Greenheugh Pediment) do see much less frequent dust lifting, but dust lifting is not strongly biased towards the lowest TI surfaces.

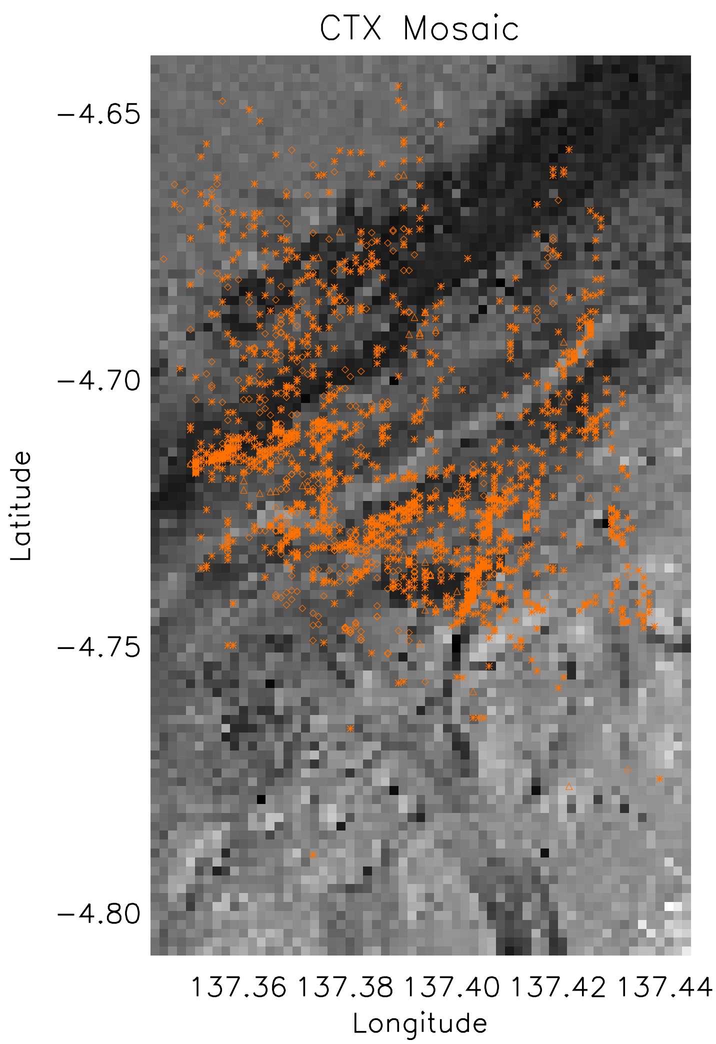

Figure 14. Dust lifting locations and symbols from Figure 13 overplotted on a 100 m resolution Context Camera mosaic of Gale Crater.

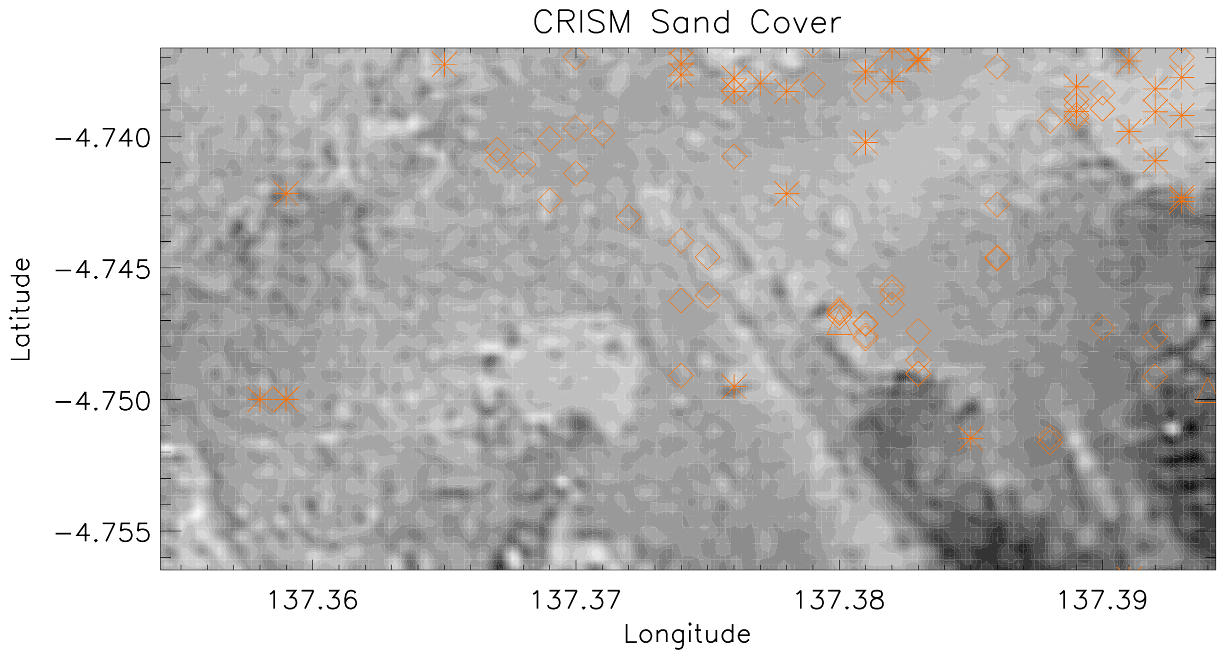

Figure 15. Dust lifting locations and symbols from Figure 13 overplotted on unitless CRISM-derived sand coverage (scaled between 0 and 1; Christian et al., 2022). Brighter terrain indicates higher sand coverage.

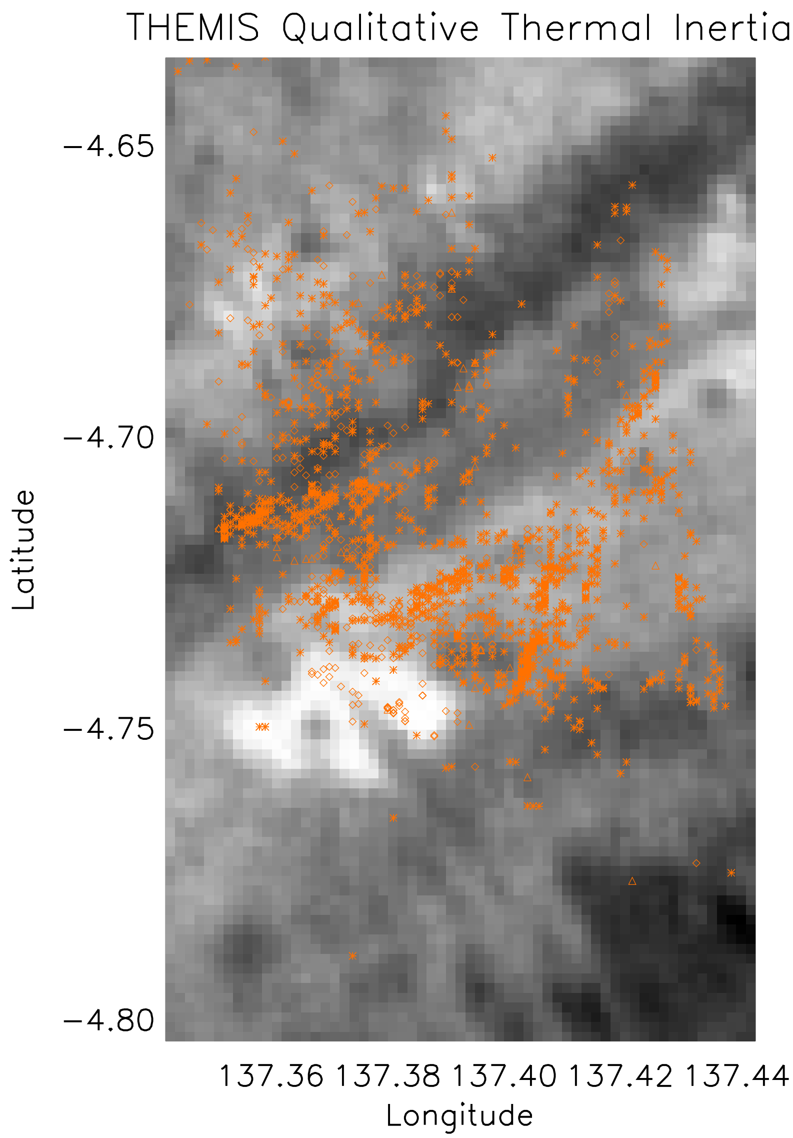

Figure 16. Dust lifting locations and symbols from Figure 13 overplotted on a 100 m resolution map of THEMIS qualitative thermal inertia. Brighter terrain indicates higher thermal inertia.

3.3. Dust Lifting Motion

Finally, we have used the Navcam dust devil image sequences to determine approximate directions of motion of some dust lifting events. Out of the entirety of the data, we were able to track approximately 750 dust lifting events across multiple images to determine motion in two orthogonal directions: across the frame (orthogonal to the image pointing azimuth) or toward or away from the rover (along the image pointing vector). For example, if a dust devil movie was taken pointing due north (azimuth 360°) and a dust devil was moving right-to-left across the field-of-view during the movie, we count that as a component of motion toward the west (azimuth 270°). If the same dust devil was also moving equally fast toward the rover, we add those two motion components and count that as moving southwest (azimuth 235°). As described by Sinclair (1969) and Balme et al. (2012), dust devils typically move with the mean wind direction, although they can tend to form curving or cycloidal tracks. Using these dust lifting event motion directions, we can estimate at least a component of the wind vector. In the example above with a west-moving dust devil, it implies a component of the wind vector from the east (azimuth 90°).

Figure 17 uses a wind rose to present the implied wind direction components across the entire ~750 dust lifting events for which we could determine motion. As with all sections in this work, we are mindful of observational biases present in these data. For example, as has been said previously, all pointing azimuths are not equally observed. Additionally, motion toward or away from the rover is far more difficult to determine from the image sequences, particularly for distant dust lifting events.

Easterly and northerly winds are the dominant implied wind directions, with a complete dearth of winds from the southwest. True easterly wind directions are the most common, representing ~25% of the total, with northeasterly winds the second most frequent. While implied southeasterly winds have been seen, true south or southwest winds were never observed. In the topography of Gale Crater along the rover's traverse, these wind directions are generally oriented along the slope of Mt. Sharp (the easterly winds) or upslope (the winds with a northerly component). Southerly or southwesterly winds would represent downslope flow. The northerly and northeasterly implied wind directions are well-matched to previously observed REMS wind directions, even though most of those data were taken prior to our Sol 1500-3800 period. Viúdez-Moreiras et al. (2019) shows a strong preference for northerly and northeasterly winds during midday (1000-1500 LTST) across the year (see their figure 9). Newman et al. (2017) similarly shows a strong bias to northerly winds when the rover was moving through the Bagnold Dunes, with supporting MarsWRF model simulations also predicting northerly and northeasterly wind directions. As those references discuss, upslope flow is expected during the day as Mt. Sharp heats up and rises due to convection and air moves upslope with anabatic wind flows to maintain hydrostatic balance. While we see easterly implied winds most often in Figure 17, true easterly winds are not common in either REMS observations or model simulations during the daytime in the vicinity of the rover's traverse. However, this discrepancy could be reconciled well if the easterly components in Figure 17 also have a northerly component (i.e., the dust lifting events also had a component of southward motion) that was not distinguishable in the images. Given that many of these implied easterly wind directions are based on dust lifting events near the Bagnold Dunes and seen from kilometers distance, this seems plausible.

Looking for variations across solar longitude or time of day, we see very little robust indications of variability in either dimension (not shown). The first half of the year (L_s = 0-180°) has a preference for more northerly or even northwesterly wind components compared to the second half of the year (L_s = 180-360°), but the broad pattern shown in Figure 17 is common across all seasons. Similarly in time of day, there is very little change (and we do not thoroughly sample all daytime hours as discussed above in Section 3.1). The most variability is across different periods of the mission as delineated in Figure 11. But we believe this variability is largely due to inherent viewshed biases present in each particular portion of the traverse which results in a strong preference to observe motion in certain directions (e.g., westerly motion/easterly wind direction when pointing north at the Bagnold Dunes), and is not due to true changes in meteorological conditions.

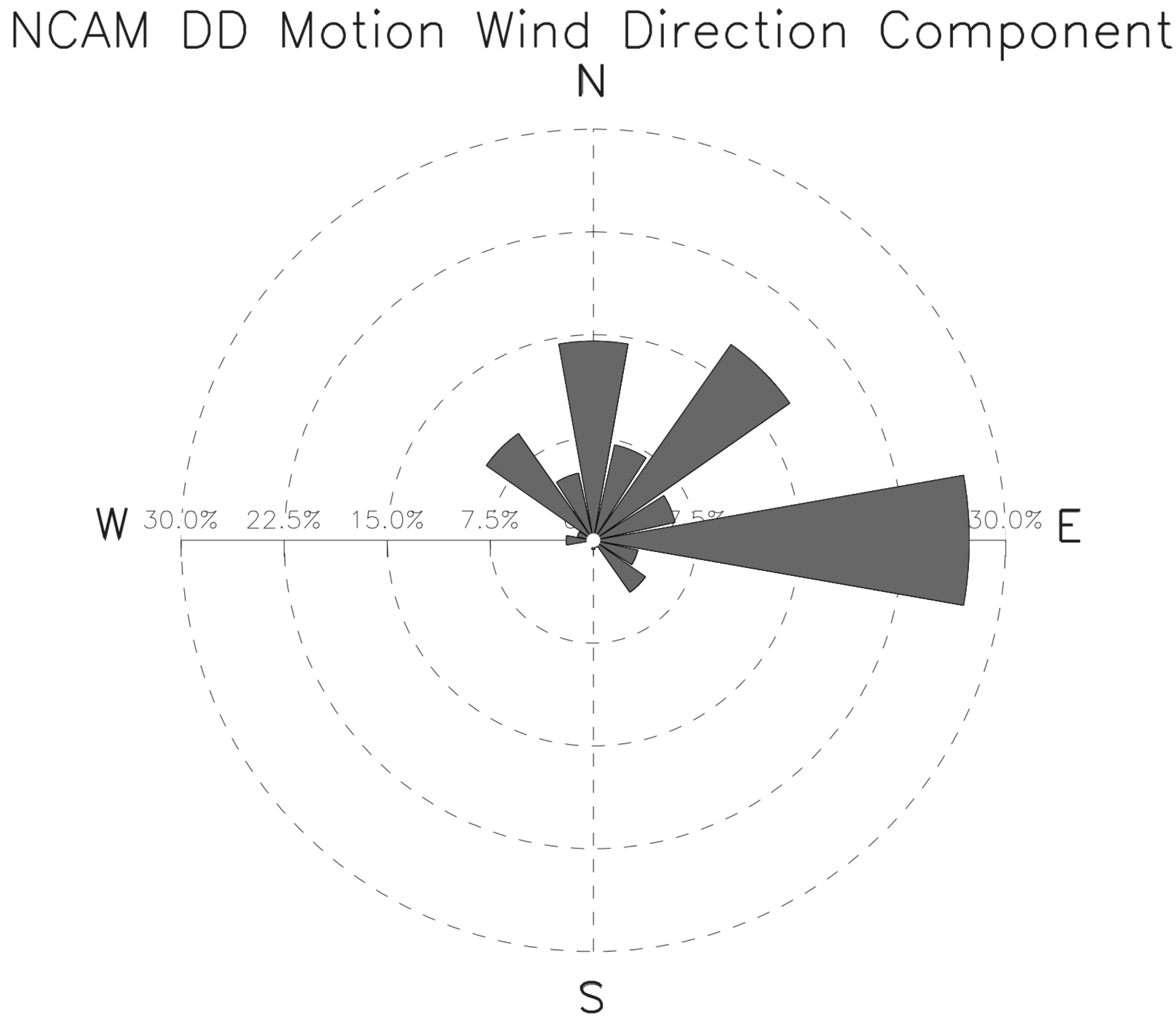

Figure 17. Wind rose diagram of implied wind direction components as determined by dust lifting event motion over the entire observation period.

4 Discussion and Conclusions

We have analyzed 1,260 Navcam image sequences to search for dust lifting in Gale Crater over MSL mission Sols 1500-3800, spanning Mars years 33-37. On average, a Navcam image sequence searching for dust lifting has been taken once every 1.8 sols during this period using a mix of three primary types of sequences: movies, surveys, and SPENDI activities (see Section 2 for descriptions). Approximately 9.5% of all images taken have included dust lifting, entailing both dust devils and wind stress forced dust lifting. Prior to Sol 1500, only a handful of dust devils was observed (Moores et al., 2015a; Lemmon et al., 2017) because images were most commonly pointed northward over the floor of Gale Crater where environmental conditions are less suitable for dust lifting (Newman et al., 2019). Dust devils comprise ~79% of all observed dust lifting events, while ~16% were classified as linear wind stress dust lifting.

Dust lifting occurs in all seasons of the martian year across the ~3.5 Mars years included in this observation period. The constantly changing viewshed of the Curiosity rover (Figure S5) as it has ascended the slopes of Mt. Sharp/Aeolis Mons have also produced significantly varying seasonal patterns to observed dust lifting in each of the complete Mars years (MY34-36) included in this observation period. Across the entire Sol 1500-3800 period, more dust lifting events have occurred in the second half of the martian year (L_s = 180-360°, southern hemisphere spring and summer), with a minimum in activity in southern hemisphere winter (L_s = 90-120°). We believe Mars Year 35 is the qualitatively most meteorologically representative year of the MSL mission, with a generally sinusoidal variation in dust lifting frequency between its peak near southern summer solstice and a minimum near winter solstice. Mars Years 34 and 36 each included events (e.g., the MY34 global dust storm) or rover positions (e.g., Marker Band Valley in the second half of MY36) that precluded or minimized dust lifting observations. This shows broad agreement with detections of convective pressure vortices by the REMS instrument (Kahanpää et al., 2016; Ordóñez-Etxeberria et al., 2018; Uttam et al., 2022; Newman et al., 2019), with more convective vortex activity during the dustier second half of the martian year. Linear wind stress dust lifting detections are strongly clustered near L_s = 180° across the 3 full Mars years in the observation period. However, these wind stress lifting detections are strongly viewshed biased. A direct comparison between the Navcam observed dust lifting events analyzed here and concurrent REMS observations is left for future work.

Observed dust lifting is clustered near local solar noon, the peak of longwave solar heating and sensible heating that drives convective instability. However, even when accounting for inherent Navcam observational biases, observed dust lifting is more strongly peaked near solar noon than was previously expected. Other factors that drive convection and vortices, such as planetary boundary layer depth, for example, peak later in the afternoon near 15:00 LTST. Dust lifting observation frequency falls sharply by 13:00 LTST and is nearly absent after 14:00 LTST. Modeling and REMS observations of convective pressure vortices show a much more gradual decline in the 12:00-14:00 LTST period, with only notable declines in activity after 15 or 16:00 LTST (Kahanpää et al., 2016; Ordóñez-Etxeberria et al., 2018; Newman et al., 2019). This suggests that meteorological conditions that support convective vortices can persist into the afternoon, while some additional factor for actual dust lifting becomes suppressive by early to mid afternoon in Gale Crater. MSL's operations played an important part in assessing the robustness of this decline in afternoon dust lifting activity. The addition of occasional low-resource "SPENDI" activities without science team involvement over the last ~900 sols has been highly valuable, and other missions should consider such activities in the future.

The varied viewsheds observed by Curiosity through this period, and other inherent biases discussed previously, make it difficult to consistently calculate a representative dust lifting event frequency or areal density for the entire mission as is described by Lorenz and Jackson (2016). However, during the Sol 2300-2900 period, Curiosity had a frequent view of the Glen Torridon valley with a cumulative viewshed area of ~6.5 km^2. As this also largely covered MY35, with the fewest inherent viewshed biases, we use 85 Navcam dust devil movies (long and short) from this period and conservatively determine a frequency of ~4.5 dust lifting events/km^2/sol. We calculate this value for the 1000-1400 LTST period, so any dust lifting at earlier or later times is not captured by this metric. This falls logarithmically half-way between the "Navcam Survey" and "Navcam Stare" values reported by Lorenz (2009) for Spirit in Gusev Crater and falls modestly below the 50/A power law fit shown by Lorenz and Jackson (2016).

The terrain of Gale Crater and Curiosity's mobility provide a unique opportunity to understand how varied surface properties influence dust lifting. We use two methods to help localize observed dust lifting. In both cases, we use the pointing information associated with each Navcam sequence, the camera's CAHVOR model, and spherical geometry to orient each image pixel in azimuth and elevation space. The simplest step is to simply report the azimuth of each dust lifting event, described above in Figure 11. The subsequent step, shown in Figures 12-16, is to project a vector from the rover's position out onto the topography of Gale Crater using the HiRISE DTM. In combination, these two methods show that dust lifting is most frequent along and in the vicinity of the Bagnold Dune field and broadly through the Glen Torridon valley. This includes both dust devils and linear wind stress dust lifting, although wind stress dust lifting is more frequent through the Bagnold Dunes and less common in the Glen Torridon valley. Dust lifting is far less frequent farther upslope on Mt. Sharp, although observational biases play a role in these statistics. Still, certain well-observed portions of Gale Crater have notable paucities of dust lifting (see Figure S5): the top of the Vera Rubin Ridge and the eastern parts of the Greenheugh Pediment and Gediz Vallis Ridge. Comparing the dust lifting locations to various maps of surface properties, there is a noticeable preference for dust lifting to occur on sandier surfaces. Throughout this observation period, Curiosity has been near or within view of the Bagnold Dune field, the Sands of Forvie sandsheet, and various other sand patches. The preference for dust lifting near sandier surfaces suggests that wind-blown sand saltating across the surface is important for dust lifting, possibly more than direct suspension of dust. Given that sandier surfaces are less dust-covered than bedrock surfaces, this implies that a high dust cover is not necessary for lifting and that available saltating sand grains are more important to splash dust particles into the atmosphere. Note also that there are thermodynamic reasons that sandy locations could also be favored for dust lifting. Low albedo and low TI basaltic sand is conducive to stronger daytime heating supportive of convection and pressure vortex formation.

Lastly, we tracked the motion of ~750 dust lifting events as a proxy for wind direction component and find broad agreement with published REMS wind direction observations (prior to the failure of the wind sensors, Viúdez-Moreiras et al., 2019; Newman et al., 2017). Throughout our observation period, there is a strong preference for implied easterly and northerly wind components. This makes intuitive sense with upslope flows expected during the midday hours when most Navcam dust devil image sequences are scheduled.

MSL operational planning routinely makes a best effort attempt to overlap scheduled Navcam image sequences with REMS measurements. In future work, we will correlate these visually detected dust lifting events with REMS meteorological observations.

Data Availability

All Navcam images are publicly available on the Planetary Data System (Maki, 2018). Guzewich et al. (2023) archives our derived dust lifting information and statistics.

Acknowledgements

We gratefully acknowledge the work of the MSL science and operations teams, particularly the Engineering Camera teams and the Environmental Science Theme Group leads. We thank John Christian for providing CRISM sand coverage data. We thank Germán Martínez, Álvaro Vicente-Retortillo, Michael Battalio, and Ashwin Vasavada for helpful suggestions, and Kathryn Steakley and Ralph Lorenz for useful reviews, that have improved this manuscript. Guzewich and Mason are supported by the MSL Participating Scientist Program.

References

Bagnold, R.A. (1936), The movement of desert sand, *Proceedings of the Royal Society of London*, 157, 594-620, https://doi.org/10.1098/rspa.1936.0218

Bagnold, R.A. (1941) The Physics of Blown Sand and Desert Dunes. Chapman and Hall, London.

Baker, M., Newman, C., Charalambous, C., Golombek, M., Spiga, A., Banfield, D., et al. (2021). Vortex-dominated aeolian activity at InSight's landing site, Part 2: Local meteorology, transport dynamics, and model analysis. *Journal of Geophysical Research: Planets*, 126, e2020JE006514. https://doi.org/10.1029/2020JE006514

Balme, M., & Greeley, R. (2006). Dust devils on Earth and Mars. *Reviews of Geophysics*, 44, RG3003. https://doi.org/10.1029/2005RG000188.

Balme, M., A. Pathare, S.M. Metzger, M.C. Towner, S.R. Lewis, A. Spiga, L.K. Fenton, N.O. Renno, H.M. Elliott, F.A. Saca, T.I. Michaels, P. Russell, and J. Verdasca (2012), Field measurements of horizontal forward motion velocities of terrestrial dust devils: Towards a proxy for ambient winds on Mars and Earth, *Icarus*, 221, 632-645, http://dx.doi.org/10.1016/j.icarus.2012.08.021.

Banfield, D. and A. Spiga, et al. (2020), The atmosphere of Mars as observed by InSight. *Nature Geoscience*, 13, 190-198.

Bennett, K. A., Hill, J. R., Murray, K. C., Edwards, C. S., Bell, J. F., & Christensen, P. R. (2018). THEMIS-VIS investigations of sand at Gale crater. *Earth and Space Science*, 5, 352–363. https://doi.org/10.1029/2018EA000380

Bennett, K. A., Fox, V. K., Bryk, A., Dietrich, W., Fedo, C., Edgar, L., et al. (2023). The Curiosity rover's exploration of Glen Torridon, Gale crater, Mars: An overview of the campaign and scientific results. *Journal of Geophysical Research: Planets*, 128, e2022JE007185. https://doi.org/10.1029/2022JE007185

Campbell, C.L., A.M. Kling, S.D. Guzewich, C.L. Smith, J.L. Kloos, M.T. Lemmon, C.A. Moore, B.A. Cooper, R.M. Haberle, and J.E. Moores (2020), Estimating the altitudes of Martian water-ice clouds above the Mars Science Laboratory rover landing site, *Planetary and Space Science*, 182, https://doi.org/10.1016/j.pss.2019.104785.

Cantor, B. A., Kanak, K. M., and Edgett, K. S. (2006), Mars Orbiter Camera observations of Martian dust devils and their tracks (September 1997 to January 2006) and evaluation of theoretical vortex models, *J. Geophys. Res.*, 111, E12002, doi:10.1029/2006JE002700.

Chapman, R.M., S.R. Lewis, M. Balme, and L.J. Steele (2017), Diurnal variation in martian dust devil activity, *Icarus*, 292, 154-167, https://10.1016/j.icarus.2017.01.003.

Charalambous, C., McClean, J. B., Baker, M., Pike, W. T., Golombek, M., Lemmon, M., et al. (2021). Vortex-dominated aeolian activity at InSight's landing site, Part 1: Multi-instrument observations, analysis, and implications. *Journal of Geophysical Research: Planets*, 126, e2020JE006757. https://doi.org/10.1029/2020JE006757

Christian, J. R., Arvidson, R. E., O'Sullivan, J. A., Vasavada, A. R., & Weitz, C. M. (2022). CRISM-based high spatial resolution thermal inertia mapping along Curiosity's traverses in Gale Crater. *Journal of Geophysical Research: Planets*, 127, e2021JE007076. https://doi.org/10.1029/2021JE007076

Clancy, R. T., Sandor, B. J., Wolff, M. J., Christensen, P. R., Smith, M. D., Pearl, J. C., Conrath, B. J., and Wilson, R. J. (2000), An intercomparison of ground-based millimeter, MGS TES, and Viking atmospheric temperature measurements: Seasonal and interannual variability of temperatures and dust loading in the global Mars atmosphere, *J. Geophys. Res.*, 105(E4), 9553– 9571, doi:10.1029/1999JE001089.

Cooper, B.A., J.E. Moores, D.J. Ellison, J.K. Kloos, C.L. Smith, S.D. Guzewich, C. L. Campbell (2018), Constraints on Mars Aphelion Cloud Belt phase function and ice crystal geometries, *Planetary and Space Science*, 168, 62-72, https://10.1016/j.pss.2019.01.055.

Di, K., and Li, R. (2004), CAHVOR camera model and its photogrammetric conversion for planetary applications, *J. Geophys. Res.*, 109, E04004, doi:10.1029/2003JE002199.

Edwards, C. S., Piqueux, S., Hamilton, V. E., Fergason, R. L., Herkenhoff, K. E., Vasavada, A. R., et al. (2018). The thermophysical properties of the Bagnold dunes, Mars: Ground-truthing orbital data. *Journal of Geophysical Research, Planets*, 123, 1307– 1326. https://doi.org/10.1029/2017JE005501

Ellehøj, M. D., Gunnlaugsson, H. P., Taylor, P. A., Kahanpää, H., Bean, K. M., Cantor, B. A., Gheynani, B. T., Drube, L., Fisher, D., Harri, A.-M., Holstein-Rathlou, C., Lemmon, M. T., Madsen, M. B., Malin, M. C., Polkko, J., Smith, P. H., Tamppari, L. K., Weng, W., & Whiteway, J. (2010). Convective vortices and dust devils at the Phoenix Mars mission landing site. *Journal of Geophysical Research*, 115, E00E16. https://doi.org/10.1029/2009JE003413.

Fenton, L., Reiss, D., Lemmon, M., Marticorena, B., Lewis, S., and B. Cantor (2016), Orbital Observations of Dust Lofted by Daytime Convective Turbulence. *Space Sci Rev* 203, 89–142, https://doi.org/10.1007/s11214-016-0243-6.

Fergason, R. L., Christensen, P. R., and Kieffer, H. H. (2006), High-resolution thermal inertia derived from the Thermal Emission Imaging System (THEMIS): Thermal model and applications, *J. Geophys. Res.*, 111, E12004, doi:10.1029/2006JE002735.

Ferri, F., P. H. Smith, M. Lemmon, and N. O. Rennó (2003), Dust devils as observed by Mars Pathfinder, *J. Geophys. Res.*, 108(E12), 5133, doi:10.1029/2000JE001421.

Fisher, J. A., M. I. Richardson, C. E. Newman, M. A. Szwast, C. Graf, S. Basu, S. P. Ewald, A. D. Toigo, and R. J. Wilson (2005), A survey of Martian dust devil activity using Mars Global Surveyor Mars Orbiter Camera images, *J. Geophys. Res.*, 110, E03004, doi:10.1029/2003JE002165.

Gómez-Elvira, J., C. Armiens, L. Castañer, M. Domínguez, M. Genzer, F. Gómez, R. Haberle, A. M. Harri, V. Jiménez, H. Kahanpää, & L. Kowalski (2012), REMS: The environmental sensor suite for the Mars Science Laboratory rover, *Space Sci. Rev*., 170(1-4), 583-640.

Greeley, R., M. R. Balme, J. D. Iversen, S. Metzger, B. Mickelson, J. Phoreman, and B. White (2003), Martian dust devils: Laboratory simulations of particle threshold, *J. Geophys. Res.*, 108(E5), 5041, doi:10.1029/2002JE001987.

Greeley, R., et al. (2006), Active dust devils in Gusev crater, Mars: Observations from the Mars Exploration Rover Spirit, *J. Geophys. Res.*, 111, E12S09, doi:10.1029/2006JE002743.

Greeley, R., Waller, D. A., Cabrol, N. A., Landis, G. A., Lemmon, M. T., Neakrase, L. D. V., Pendleton Hoffer, M., Thompson, S. D., and Whelley, P. L. (2010), Gusev Crater, Mars: Observations of three dust devil seasons, *J. Geophys. Res.*, 115, E00F02, doi:10.1029/2010JE003608.

Guzewich, Scott, Mason, Emily, Lemmon, Mark, Newman, Claire, & Lewis, Kevin. (2023). Dust Lifting Observations with the Mars Science Laboratory Navigation Cameras. https://doi.org/10.5281/zenodo.83344947.

Guzewich, S.D., A.D. Toigo, L. Kulowski, H. Wang (2015), Mars Orbiter Camera climatology of textured dust storms, Icarus, 258, 1-13, doi: 10.1016/j.icarus.2015.06.023.

Guzewich, S.D., M. Lemmon, C.L. Smith, G. Martínez, Á. De Vicente-Retortillo, C.E. Newman, M. Baker, C. Campbell, B. Cooper, J. Gómez-Elvira, A.-M. Harri, D. Hassler, F.J. Martin-Torres, T. McConnochie, J.E. Moores, H. Kahanpää, A. Khayat, M.I. Richardson, M.D. Smith, R. Sullivan, M. de la Torre Juarez, A.R. Vasavada, D. Viúdez-Moreiras, C. Zeitlin, M.-P. Zorzano Mier (2019), Mars Science Laboratory Observations of the 2018/Mars Year 34 Global Dust Storm, Geophysical Research Letters, 46(1), 71-79, https://doi.org/10.1029/2018GL080839.

Harri, A.-M., M. Genzer, O. Kemppinen, H. Kahnapää, J. Gomez-Elvira, J.A. Rodriguez-Manfredi, R. Haberle, J. Polkko, W. Schmidt, H. Savijärvi, J. Kauhanen, E. Atlaskin, M. Richardson, T. Siili, M. Paton, M. de La Torre- Juarez, C. Newman, S. Rafkin, M.T. Lemmon, M. Mischna, S. Merikallio, H. Haukka, J. Martin-Torres, M.-P. Zorzano, V. Peiñado, R. Urqui, A. Lepinette, A. Scodary, T. Mäkinen, L. Vazquez, N. Rennó, and the REMS/MSL Science Team (2014), Pressure observations by the Curiosity rover: Initial results, *Journal of Geophysical Research Planets*, 119(1):82-92, doi:10.1002/2013JE004423.

Hayes, C. W., J.K. Kloos, A.C. Innanen, C.L. Campbell, H.M. Spears, and J.E. Moores (2023), Five Mars Years of Cloud Observations at Gale Crater: Opacities, Variability, and Ice Crystal Habits, *Planetary Science Journal*, in review.

Hueso, R., Newman, C. E., del Río-Gaztelurrutia, T., Munguira, A., Sánchez-Lavega, A., Toledo, D., et al. (2023). Convective vortices and dust devils detected and characterized by

Mars 2020. *Journal of Geophysical Research: Planets*, 128, e2022JE007516. https://doi.org/10.1029/2022JE007516

Jackson, B., J. Crevier, M. Szurgot, R. Battin, C. Perrin, S. Rodriguez (2021), Inferring Vortex and Dust Devil Statistics from InSight, *The Planetary Science Journal*, 10.3847/PSJ/ac260d, 2, 5, (206).

Jackson, B. (2022), Vortices and Dust Devils as Observed by the Mars Environmental Dynamics Analyzer Instruments Onboard the Mars 2020 Perseverance Rover, *Planetary Science Journal*, 3, 20, doi: 10.3847/PSJ/c4586.

Kahanpää, H., Newman, C. E., Moores, J., Zorzano, M.-P., Martín-Torres, J., Navarro, S., Lepinette, A., Cantor, B., Lemmon, M. T., Valentín-Serrano, P., Ullán, A., & Schmidt, W. (2016). Convective vortices and dust devils at the MSL landing site: Annual variability. *Journal of Geophysical Research: Planets*, 121, 1514– 1549. https://doi.org/10.1002/2016JE005027.

Kahanpää, H. and D. Viúdez-Moreiras (2021), Modelling martian dust devils using in-situ wind, pressure, and UV radiation measurements by Mars Science Laboratory, *Icarus*, 359, 114207, doi: 10.1016/j.icarus/2020.114207.

Kahre, M. et al. (2017), The Mars Dust Cycle. In The Atmosphere and Climate of Mars, Cambridge University Press.

Kirk, R. L., et al. (2008), Ultrahigh resolution topographic mapping of Mars with MRO HiRISE stereo images: Meter-scale slopes of candidate Phoenix landing sites, *J. Geophys. Res.*, 113, E00A24, doi:10.1029/2007JE003000.

Kloos, J. L., Moores, J. E., Lemmon, M., Kass, D., Francis, R., de la Torre Juárez, M., … Martín-Torres, F. J. (2016). The first Martian year of cloud activity from Mars Science Laboratory (sol 0–800). *Advances in Space Research*, 57(5), 1223– 1240.

Kloos, J. L., Moores, J. E., Whiteway, J. A., & Aggarwal, M. (2018). Interannual and diurnal variability in water ice clouds observed from MSL over two Martian years. *Journal of Geophysical Research: Planets*, 123, 233– 245. https://doi.org/10.1002/2017JE005314.

Kok, J.F., Parteli, E.J.R, Michaels, T.I., Karam, D.B. (2012), The physics of wind-blown sand and dust, *Reports on Progress in Physics*, 10.1088/0034-4885/75/10/106901, 75, 10, (106901).

Lemmon, M.T. and C.E. Newman, N. Rennon, E. Mason, M. Battalio, M.I. Richardson, and H. Kahanpää (2017), Dust Devil Activity at the Curiosity Mars Rover Field Site, presented at the 48th Lunar and Planetary Science Conference, #2952, The Woodlands, TX, USA.

Lemmon, M. T., Smith, M. D., Viudez-Moreiras, D., de la Torre-Juarez, M., Vicente-Retortillo, A., Munguira, A., et al. (2022). Dust, sand, and winds within an active Martian storm in Jezero crater. *Geophysical Research Letters*, 49, e2022GL100126. https://doi.org/10.1029/2022GL100126

Lorenz, R.D. (2009), Power law of dust devil diameters on Mars and Earth, *Icarus*, 203(2), 683-684, https://doi.org/10.1016/j.icarus.2009.06.029.

Lorenz, R. D. (2014). Vortex Encounter Rates with Fixed Barometer Stations: Comparison with Visual Dust Devil Counts and Large-Eddy Simulations, *Journal of the Atmospheric Sciences*, *71*(12), 4461-4472.

Lorenz, R. D., and B. K. Jackson (2015), Dust devils and dustless vortices on a desert playa observed with surface pressure and solar flux logging, *Geo Res J*, 5, 1– 11.

Lorenz, R.D., Jackson, B.K. Dust Devil Populations and Statistics. *Space Sci Rev* **203**, 277–297 (2016). https://doi.org/10.1007/s11214-016-0277-9

Lorenz, R. D. (2016). Heuristic estimation of dust devil vortex parameters and trajectories from single-station meteorological observations: Application to InSight at Mars. *Icarus*, 271, 326–337. https://doi.org/10.1016/j.icarus.2016.02.001.

Lorenz, R. D., Spiga, A., Lognonne, P., Plasman, M., Newman, C. E., & Charalam-Bous, C. (2020). The whirlwinds of Elysium: A catalog and meteorological characteristics of “dust devil” vortices observed by Insight on Mars. *Icarus*, 355, https://doi.org/10.1016/j.icarus.2020.114119.

Lorenz, R.D., M.T. Lemmon, J. Maki (2021a), First Mars year of observations with the InSight solar arrays: Winds, dust devil shadows, and dust accumulation, *Icarus*, 364, 114468, https://10.1016/j.icarus.2021.114468.

Lorenz, R.D., G. Martínez, A. Spiga, A. Vicente-Retortillo, C.E. Newman, N. Murdoch, F. Forget, E. Millour, and T. Pierron (2021b), Lander and rover histories of dust accumulation on and removal from solar arrays on Mars, Planetary and Space Science, 207, 105337, https://doi.org/10.1016/j.pss.2021.105337.

Mason, E.M., M.D. Smith, M.I. Richardson, and S.D. Guzewich (2023), Comparing Atmospheric Temperature Fluctuations Across Landed Missions as a Diagnostic of Boundary Layer Activity, *Journal of Geophysical Research-Planets*, in review.

Maki, J. N., et al. (2003), Mars Exploration Rover Engineering Cameras, *J. Geophys. Res.*, 108, 8071, doi:10.1029/2003JE002077, E12.

Maki, J.N., D. Thiessen, A. Pourangi, P. Kobzeff, T. Litwin, L. Scherr, S. Elliot, A. Dingizian, M. Maimone (2012). The Mars Science Laboratory Engineering Cameras, *Space Sci. Rev.*, DOI 10.1007/s11214-012-9882-4.

Maki, J. (2018). MSL MARS NAVIGATION CAMERA 5 RDR V2.0 [Data set]. NASA Planetary Data System. https://doi.org/10.17189/1519572

Martínez, G. M., Vicente-Retortillo, A., Vasavada, A. R., Newman, C. E., Fischer, E., Rennó, N. O., et al. (2021). The surface energy budget at Gale crater during the first 2500 sols of the Mars Science Laboratory mission. Journal of Geophysical Research: Planets, 126, e2020JE006804, doi: 10.1029/2020JE006804

Metzger, S. M., J. R. Carr, J. Johnson, T. Parker, and M. Lemmon (1999), Dust devil vortices as seen by the Mars Pathfinder Camera, *Geophys. Res. Lett.*, 26, 2781–2784

Metzger, S.M., J.R. Carr, J.R. Johnson, T.J. Parker, and M.T. Lemmon (2000), Techniques for identifying dust devils in Mars Pathfinder images, IEEE Transactions on Geosciences, 38(2), 870-876, doi: 10.1109/36.842015.

Moore, C. A., Moores, J. E., Lemmon, M. T., Rafkin, S. C. R., Francis, R., Pla-García, J., Haberle, R. M., Zorzano, M.-P., Martín-Torres, F. J., & Burton, J. R. (2016). A full martian year of line-of-sight extinction within Gale Crater, Mars as acquired by the MSL Navcam through sol 900. *Icarus*, 264, 102– 108.

Moore, C. A., Moores, J. E., Newman, C. E., Lemmon, M. T., Guzewich, S. D., & Battalio, M. (2019). Vertical and horizontal heterogeneity of atmospheric dust loading in northern Gale Crater, Mars. *Icarus*, 329, 197– 206. https://doi.org/10.1016/j.icarus.2019.03.041

Moores, J.E. et al. (2015) Observational evidence of a suppressed planetary boundary layer in northern Gale Crater, Mars as seen by the Navcam instrument onboard the Mars Science Laboratory rover. *Icarus* v. 249 pp.129-142 Doi: 10.1016/j.icarus.2014.09.020

Moores, J. E., Lemmon, M. T., Rafkin, S. C., Francis, R., Pla-Garcia, J., Torre, M. D. L., … McCullough, E.(2015). Atmospheric movies acquired at the Mars Science Laboratory landing site: Cloud morphology, frequency and significance to the Gale Crater water cycle and Phoenix mission results. *Advances in Space Research*, 55(9), 2217– 2238.

Murdoch, N., Stott, A.E., Gillier, M. *et al.* (2022), The sound of a Martian dust devil. *Nat Commun,* 13, 7505, https://doi.org/10.1038/s41467-022-35100-z

Neakrease, L.D.V. and R. Greeley (2010), Dust devil sediment flux on Earth and Mars: Laboratory simulations, *Icarus*, 206(1), 306-218, https://doi.org/10.1016/j.icarus.2009.08.028.

Neakrase, L. D. V., Balme, M. R., Esposito, F., Kelling, T., Klose, M., Kok, J. F., Marticorena, B., Merrison, J., Patel, M., & Wurm, G. (2016). Particle lifting processes in dust devils. *Space Science Reviews*,203(347). https://doi.org/10.1007/s11214-016-0296-6.

Newman, C.E., J. Gómez-Elvira, M. Marin, S. Navarro, J. Torres, M.I. Richardson, J.M. Battalio, S.D. Guzewich, R. Sullivan, M. de la Torre, A.R. Vasavada, and N.T. Bridges (2017), Winds measured by the Rover Environmental Monitoring Station (REMS) during the Mars Science Laboratory (MSL) rover's Bagnold Dunes Campaign and comparison with numerical modeling using MarsWRF, *Icarus*, 291:203-231, doi: 10.1016/j.icarus.2016.12.016.

Newman, C.E., H. Kahanpää, M.I. Richardson, G.M. Martinez, A. Vicente-Retortillo, and M. Lemmon (2019), MarsWRF Convective Vortex and Dust Devil Predictions for Gale Crater Over 3 Mars Years and Comparison with MSL-REMS Observations, *Journal of Geophysical Research Planets*, 124(12):3442-3468, doi:10.1029/2019JE006082.

Newman, C.E., R.Hueso, M. T. Lemmon, A. Munguira, Á. Vicente-Retortillo, V. Apestigue, G. M. Martínez, D.Toledo, R. Sullivan, K. E. Herkenhoff, M. de la Torre Juárez, M. I. Richardson, A. E. Stott, N. Murdoch, A.Sanchez-Lavega, M.J. Wolff, I. Arruego, E. Sebastián, S. Navarro, J.Gómez-Elvira, L. Tamppari, M. D. Smith, A. Lepinette, D.Viúdez-Moreiras, A.-M. Harri, M. Genzer, M.Hieta, R. D. Lorenz, P. Conrad, F. Gómez, T. H. McConnochie, D. Mimoun, C. Tate, T. Bertrand, J. F. Bell, J. N. Maki, J. A. Rodriguez-Manfredi, R. C. Wiens, B. Chide, S. Maurice, M.-P. Zorzano, L. Mora, M. M. Baker, D. Banfield, J. Pla-Garcia, O. Beyssac, A. Brown, B. Clark, F. Montmessin, E. Fischer, P. Patel, T. del Río-Gaztelurrutia, T. Fouchet, R. Francis, S. D. Guzewich (2022), The dynamic atmospheric and aeolian environment of Jezero crater, Mars, *Science Advances*, 10.1126/sciadv.abn3783, 8, 21.

Ordóñez-Etxeberria, I., Hueso, R., & Sánchez-Lavega, A. (2018). A systematic search of sudden pressure drops on Gale crater during two Martian years derived from MSL/REMS data. *Icarus*, 299, 309– 330. https://doi.org/10.1016/j.icarus.2017.07.0320019-1035.

Ordóñez-Etxeberria, I., Hueso, R., & Sánchez-Lavega, A. (2020). Strong increase in dust devil activity at Gale Crater on the third year of the MSL mission and suppression during the 2018 Global Dust Storm. *Icarus*, 299, 309– 330. doi: 10.1016/j.icarus.2020.113814.

Reiss, D. N.M. Hoekzema, and O.J. Stenzel (2014), Dust deflation by dust devils on Mars derived from optical depth measurements using the shadow method in HiRISE images, *Planetary and Space Science*, 93-94, 54-65, https://doi.org/10.1016/j.pss.2014.01.016.

Rennó, N. O., M. L. Burkett, and M. P. Larkin, 1998: A Simple Thermodynamical Theory for Dust Devils. *J. Atmos. Sci.*, **55**, 3244–3252, https://doi.org/10.1175/1520-0469(1998)055<3244:ASTTFD>2.0.CO;2.

Ringrose, T.J., M.C. Towner, and J.C. Zarnecki (2003), Convective vortices on Mars: a reanalysis of Viking Lander 2 meteorological data, sols 1–60. *Icarus* 163, 78–87, doi:10.1016/S0019-1035(03)00073-3

Ringrose T.J. (2005), Inside dust devils, *Astronomy & Geophysics*, Volume 46, Issue 5, 5.16–5.19, https://doi.org/10.1111/j.1468-4004.2005.46516.x

Robbins, S. J., Kirchoff, M. R., & Hoover, R. H. (2023). Fully controlled 6 meters per pixel equatorial mosaic of Mars from *Mars Reconnaissance Orbiter* Context Camera images, version 1. *Earth and Space Science*, 10, e2022EA002443. https://doi.org/10.1029/2022EA002443

Ryan, J. A., and Carroll, J. J. (1970), Dust devil wind velocities: Mature state, *J. Geophys. Res.*, 75(3), 531– 541, doi:10.1029/JC075i003p00531.

Ryan, J.A. and R.D. Lucich (1983), Possible dust devils, vortices on Mars. *J. Geophys. Res.* 88(C15), 11005–11011, doi:10.1029/JC088iC15p11005

Sagan, C., Bagnold, R.A. (1975), Fluid transport on Earth and aeolian transport on Mars. Icarus 26 (2), 209–218. https://doi.org/10.1016/0019-1035(75)90080-9.

Schofield, J. T., J. R. Barnes, D. Crisp, R. M. Haberle, S. Larsen, J. A. Magalhaes, J. R. Murphy, A. Seiff, and G. Wilson (1997), The Mars Pathfinder Atmospheric Structure Investigation/Meteorology (ASI/MET) experiment, *Science*, 278, 1752– 1758.

Sinclair, P.C. (1969), General characteristics of dust devils, *Journal of Applied Meteorology*, 8, 32-45.

Smith, C. L., Moores, J. E., Lemmon, M., Guzewich, S. D., Moore, C. A., Ellison, D., & Khayat, A. S. J. (2019). Visibility and line-of-sight extinction estimates in Gale Crater during the 2018/MY34 global dust storm. *Geophysical Research Letters*, 46, 9414– 9421. https://doi.org/10.1029/2019GL083788

Spiga, A., Murdoch, N., Lorenz, R., Forget, F., Newman, C., Rodriguez, S., et al. (2021). A study of daytime convective vortices and turbulence in the Martian planetary boundary layer based on half-a-year of InSight atmospheric measurements and large-eddy simulations. *Journal of Geophysical Research: Planets*, 126, e2020JE006511. https://doi.org/10.1029/2020JE006511

Stanzel, C., Pätzold, M., Greeley, R., Hauber, E., and Neukum, G. (2006), Dust devils on Mars observed by the High Resolution Stereo Camera, *Geophys. Res. Lett.*, 33, L11202, doi:10.1029/2006GL025816.

Steakley, K. and J. Murphy (2016), A year of convective vortex activity at Gale Crater, *Icarus*, 278, 180-193, doi: 10.1016/j.icarus.2016.06.010.

Sullivan, R., Baker, M., Newman, C., Turner, M., Schieber, J., Weitz, C., et al. (2022). The aeolian environment in Glen Torridon, Gale crater, Mars. *Journal of Geophysical Research: Planets*, 127, e2021JE007174. https://doi.org/10.1029/2021JE007174

Thomas, P., and P. J. Gierasch (1985), Dust devils on Mars, *Science*, 230, 175–177.

Toledo, D., Apéstigue, V., Arruego, I., Lemmon, M., Gómez, L., Montoro, F., et al. (2023). Dust devil frequency of occurrence and radiative effects at Jezero crater, Mars, as measured by MEDA Radiation and Dust Sensor (RDS). *Journal of Geophysical Research: Planets*, *128*, e2022JE007494. https://doi. org/10.1029/2022JE007494

Vasavada, A.R., S. Piqueux, K.W. Lewis, M.T. Lemmon, and M.D. Smith (2017), Thermophysical properties along Curiosity's traverse in Gale Crater, Mars, derived from the REMS ground temperature sensor, Icarus, 284, 372-386, https://10.1016/j.icarus.2017.11.035.

Vasavada, A.R. (2022), Mission Overview and Scientific Contributions from the Mars Science Laboratory Curiosity Rover After Eight Years of Surface Operations. *Space Sci Rev* 218, 14, https://doi.org/10.1007/s11214-022-00882-7

Vicente-Retortillo, Á., Martínez, G.M., Rennó, N. *et al.* (2018), Seasonal Deposition and Lifting of Dust on Mars as Observed by the Curiosity Rover. *Sci Rep* 8, 17576, doi:10.1038/s41598-018-35946-8.

Vicente-Retortillo, Á., Martínez, G.M., Rennó, N.O. et al. (2020), In Situ UV Measurements by MSL/REMS: Dust Deposition and Angular Response Corrections. *Space Sci Rev* 216, 97, doi: 10.1007/s11214-020-00722-6.

Vicente-Retortillo, Á., Martínez, G. M., Lemmon, M. T., Hueso, R., Johnson, J. R., Sullivan, R., et al. (2023). Dust lifting through surface albedo changes at Jezero Crater, Mars. Journal of Geophysical Research: Planets, 128, e2022JE007672, doi: 10.1029/2022JE007672.

Viúdez-Moreiras, D., Gómez-Elvira, J., Newman, C. E., Navarro, S., Marin, M., Torres, J., et al. (2019a). Gale surface wind characterization based on the Mars Science Laboratory REMS dataset. Part I: Wind retrieval and Gale's wind speeds and directions. *Icarus*, 319, 909– 925. https://doi.org/10.1016/j.icarus.2018.10.011

Viviano-Beck, C. E., Seelos, F. P., Murchie, S. L., Kahn, E. G., Seelos, K. D., Taylor, H. W., et al. (2014). Revised CRISM spectral parameters and summary products based on the currently detected mineral diversity on Mars. *Journal of Geophysical Research: Planets*, 119(6), 1403–1431. https://doi.org/10.1002/2014JE004627

Uttam, S., V. Sheel, D. Singh, C.E. Newman, and M.T. Lemmon (2022), Characteristics of convective vortices and dust devils at gale crater on Mars during MY33, *Planetary and Space Science*, 213, 105430, https://doi.org/10.1016/j.pss.2022.105430.

Whelley, P. L., and Greeley, R. (2008), The distribution of dust devil activity on Mars, *J. Geophys. Res.*, 113, E07002, doi:10.1029/2007JE002966.

Wu, Z., Richardson, M. I., Zhang, X., Cui, J., Heavens, N. G., Lee, C., et al. (2021). Large eddy simulations of the dusty Martian convective boundary layer with MarsWRF. *Journal of Geophysical Research: Planets*, 126(9), e06752.